

Improving Simulations of Convective Systems from TRMM LBA: Easterly and Westerly Regimes

S. LANG,* W.-K. TAO,+ R. CIFELLI,# W. OLSON,@ J. HALVERSON,@ S. RUTLEDGE,#
AND J. SIMPSON+

* *Laboratory for Atmospheres, NASA Goddard Space Flight Center, Greenbelt, and Science Systems and Applications, Inc., Lanham, Maryland*

+ *Laboratory for Atmospheres, NASA Goddard Space Flight Center, Greenbelt, Maryland*

Department of Atmospheric Science, Colorado State University, Fort Collins, Colorado

@ *Laboratory for Atmospheres, NASA Goddard Space Flight Center, Greenbelt, and Joint Center for Earth Systems Technology, University of Maryland, Baltimore County, Baltimore, Maryland*

(Manuscript received 18 November 2005, in final form 13 July 2006)

ABSTRACT

The 3D Goddard Cumulus Ensemble model is used to simulate two convective events observed during the Tropical Rainfall Measuring Mission Large-Scale Biosphere–Atmosphere (TRMM LBA) experiment in Brazil. These two events epitomized the type of convective systems that formed in two distinctly different environments observed during TRMM LBA. The 26 January 1999 squall line formed within a sheared low-level easterly wind flow. On 23 February 1999, convection developed in weak low-level westerly flow, resulting in weakly organized, less intense convection. Initial simulations captured the basic organization and intensity of each event. However, improvements to the model resolution and microphysics produced better simulations as compared to observations. More realistic diurnal convective growth was achieved by lowering the horizontal grid spacing from 1000 to 250 m. This produced a gradual transition from shallow to deep convection that occurred over a span of hours as opposed to an abrupt appearance of deep convection. Eliminating the dry growth of graupel in the bulk microphysics scheme effectively removed the unrealistic presence of high-density ice in the simulated anvil. However, comparisons with radar reflectivity data using contoured-frequency-with-altitude diagrams (CFADs) revealed that the resulting snow contents were too large. The excessive snow was reduced primarily by lowering the collection efficiency of cloud water by snow and resulted in further agreement with the radar observations. The transfer of cloud-sized particles to precipitation-sized ice appears to be too efficient in the original scheme. Overall, these changes to the microphysics lead to more realistic precipitation ice contents in the model. However, artifacts due to the inability of the one-moment scheme to allow for size sorting, such as excessive low-level rain evaporation, were also found but could not be resolved without moving to a two-moment or bin scheme. As a result, model rainfall histograms underestimated the occurrence of high rain rates compared to radar-based histograms. Nevertheless, the improved precipitation-sized ice signature in the model simulations should lead to better latent heating retrievals as a result of both better convective–stratiform separation within the model as well as more physically realistic hydrometeor structures for radiance calculations.

1. Introduction

Cloud models serve as a valuable tool for inferring information about clouds that cannot be directly measured such as latent heating (Tao et al. 1990, 1993b, 2000, 2001; Olson et al. 1999; Yang and Smith 1999a,b, 2000; Shige et al. 2004), budget sensitivities (Tao et al. 1993a), cloud–radiation interaction (Tao et al. 1996),

and remote sensing of precipitation (Szejwach et al. 1986; Mugnai et al. 1990, 1993; Adler et al. 1991; Smith et al. 1992, 1994; Kummerow et al. 1996; Panegrossi et al. 1998; Olson et al. 2006). Furthermore, these models provide a means to improve deficiencies in larger-scale models. A central objective of the Global Energy and Water-Cycle Experiment (GEWEX) Cloud System Study (GCSS) is to improve the parameterization of cloud systems in large-scale models by improving our understanding of cloud system processes using cloud-resolving models (CRMs; Moncrieff et al. 1997). It is imperative therefore that CRM results are carefully verified with observational data to ensure that the in-

Corresponding author address: Mr. Stephen Lang, Mesoscale Atmospheric Processes Branch, Code 613.1, NASA Goddard Space Flight Center, Greenbelt, MD 20771.
E-mail: lang@agnes.gsfc.nasa.gov

formation being inferred/obtained from them is of the highest possible quality and as true a representation of nature as possible. Consequently, observed data should and could be used more fully to improve CRMs by identifying biases within the models and guiding needed adjustments to their physics and parameters to mitigate those biases.

The central objectives of the Tropical Rainfall Measuring Mission (TRMM; Simpson et al. 1988, 1996) are to accurately measure rainfall, its distribution and associated latent heating over the global Tropics. In support of TRMM, the following field campaigns were conducted as part of an overall validation effort: the Texas–Florida Underflight Experiments A and B (TEFLUN-A and TEFLUN-B), South China Sea Monsoon Experiment (SCSMEX), TRMM Large-Scale Biosphere–Atmosphere Experiment in Amazonia (TRMM LBA), and Kwajalein Experiment (KWAJEX). These field experiments were designed in part to improve CRMs (Kummerow et al. 2000) as CRMs serve as the fundamental tool used to convert TRMM measurements into estimates of latent heating. A crucial component of the field campaigns, therefore, included collecting datasets that could be used to both initialize and validate CRMs.

TRMM LBA was conducted in January and February of 1999 in Rondonia, Brazil, to measure the dynamical, microphysical, electrical, and diabatic heating characteristics of wet season, tropical continental convection in the region. TRMM LBA employed a variety of instrumentation including the National Aeronautics and Space Administration (NASA) Tropical Oceans Global Atmosphere (TOGA) radar, the National Center for Atmospheric Research (NCAR) S-band dual-polarization Doppler radar (S-Pol), a sounding network of four radiosonde sites, three tethered sites, two flux towers, two profilers, the NASA ER-2 and University of North Dakota Citation aircraft, a lightning network, disdrometers, and a rain gauge network (Silva Dias et al. 2002a). In addition, there were overpasses by the TRMM satellite. Data from these platforms provide a valuable means for initializing and validating CRMs by measuring environmental and storm characteristics. This study will use a CRM to simulate convection from TRMM LBA. Thus, radiosonde data will be used for obtaining initial conditions, but the focus will be on radar data for model evaluation.

Convection observed during TRMM LBA fell into two distinct regimes based on the low-level wind direction: an easterly regime wherein more intense, electrified, organized convective systems propagated from the east and a westerly regime wherein convection was weaker, less-organized, more widespread, and propa-

gated slowly from the west (Halverson et al. 2002; Rickenbach et al. 2002; Williams et al. 2002). The two regimes are a result of modulations in the large-scale flow pattern over South America, namely the presence or absence of stationary fronts associated with the South Atlantic convergence zone (SACZ; Rickenbach et al. 2002). In the westerly regime, northwesterly winds ahead of a stationary frontal zone enhance the transport of moisture from the deep Tropics into the region. An active SACZ, which extends northwestward into central Brazil and whose axis is located east of the TRMM LBA domain, results in stronger convergence over the Amazon Basin and more efficient transport of moisture from the deep Tropics (Herdies et al. 2002). In the easterly regime, which is associated with non-SACZ periods, northeasterly flow from the South Atlantic high penetrates across the TRMM LBA domain all the way to the foothills of the Andes. The non-SACZ periods are marked by transient frontal systems that do not penetrate as deeply into the Tropics.

The boundary layer (Betts et al. 2002) and upper-air (Halverson et al. 2002) characteristics of the two regimes have been carefully examined. Halverson et al. (2002) found that the composite easterly regime environment had 1500 J kg^{-1} of convective available potential energy (CAPE) while the mean westerly regime environment had 1000 J kg^{-1} . The easterly regime environment also tended to be weakly capped with stronger and deeper shear and was drier at lower and middle levels than the westerly regime environment. These differences in environmental conditions manifest themselves as distinct differences in the observed characteristics of the convection associated with these two regimes (Cifelli et al. 2002, 2004; Petersen et al. 2002; Rickenbach et al. 2002).

In this study, a CRM, the Goddard Cumulus Ensemble (GCE) model is used to simulate convective systems from both the easterly and westerly regimes. Silva Dias et al. (2002b) used the Regional Atmospheric Modeling System (RAMS; Pielke et al. 1992) at 2-km horizontal resolution to simulate convection from 7 February 1999, a transition day between westerly and easterly regimes. Their main emphasis was to assess the impact of topography and deforestation on initial convective development under conditions of weak large-scale forcing. The objectives of this study are to simulate the key characteristics of both easterly and westerly regime convection and obtain quality cloud datasets by carefully evaluating the simulations against radar data. Specifically, the impact on hydrometeor and apparent heating (Q_1) profiles and rainfall histograms to changes in model horizontal resolution and microphysics are evaluated using contoured frequency with altitude dia-

grams (CFADs; Yuter and Houze 1995) of radar-derived quantities. The paper is organized as follows. Section 2 briefly describes the easterly and westerly regime cases. Section 3 provides details on the model, the numerical experiments and the manner in which convection is initiated in each regime. The results are presented in section 4, including a statistical comparison against radar observations. Finally, section 5 contains the summary and conclusions.

2. LBA cases

a. 26 January 1999

The 26 January 1999 case is an example of an easterly regime mesoscale convective system (MCS) that propagated into the TRMM LBA domain from the northeast. It exhibited the features of a leading line, trailing stratiform (e.g., Houze 1977; Zipser 1977; Leary and Houze 1979; Gamache and Houze 1982; Smull and Houze 1985, 1987a,b; Chong et al. 1987; Rutledge et al. 1988). Figure 1a shows a radar constant altitude plan position indicator (CAPPI) at 2020 UTC of the 26 January MCS at an altitude of 4 km overlaid with dual-Doppler winds. A band of rather intense convective cells, with reflectivities exceeding 50 dBZ, is along the leading edge trailed by a broader area of weaker echoes. The system originated from an old outflow boundary associated with prior convection well to the northeast of the TRMM LBA domain and propagated toward the southwest before reaching the dual-Doppler region at around 1950 UTC (Cifelli et al. 2002). The convective leading edge of the system was oriented essentially north–south, perpendicular to the midlevel wind maximum and low-level shear (see Fig. 2a for the vertical wind profile). This orientation has been documented in previous studies (e.g., Barnes and Sieckman 1984; Rotunno et al. 1988; LeMone et al. 1998). Initially, the line had very little trailing stratiform area as it entered the radar domain. As the system continued westward through the radar domain, it developed a broader trailing stratiform region. By 2130 UTC, the line merged with several smaller cells out ahead of it and became oriented northwest–southeast. Finally, the system entered its decaying stage, and its convection quickly died out after 2300 UTC. By 0100 UTC 27 January, the system was devoid of convection and completely dominated by stratiform. This evolution follows the pattern described by Leary and Houze (1979).

b. 23 February 1999

The convective organization on 23 February 1999 was decidedly different. Convection was only weakly organized, as environmental winds were light (see Fig.

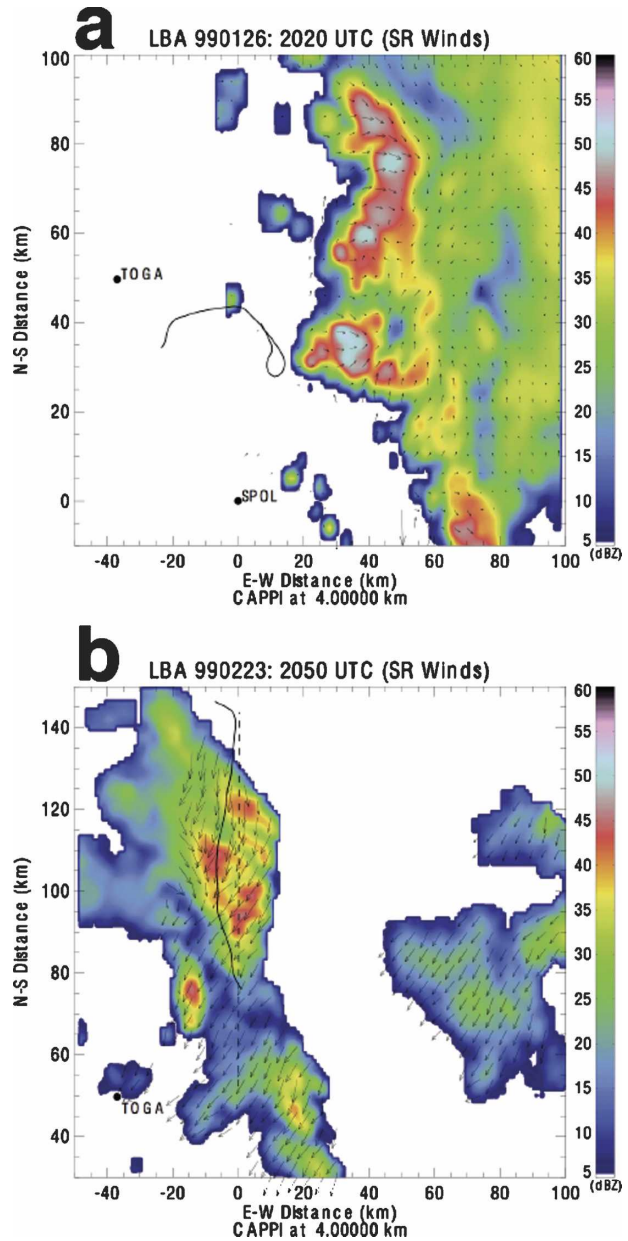


FIG. 1. Radar CAPPIs of reflectivity (dBZ) at an altitude of 4.0 km AGL at (a) 2020 UTC for the 26 Jan 1999 MCS and (b) 2050 UTC for the 23 Feb 1999 MCS. Overlaid vectors indicate storm-relative winds based on dual-Doppler wind analysis. The solid black line marks the track of the University of North Dakota (UND) Citation aircraft.

2b for the vertical wind profile). Convection broke out over a wide area in association with daytime heating and eventually formed into transient lines parallel to the deep tropospheric shear vector. This type of shear-parallel organization in the presence of weak shear conditions has been described by Barnes and Sieckman (1984), Alexander and Young (1992), and LeMone et

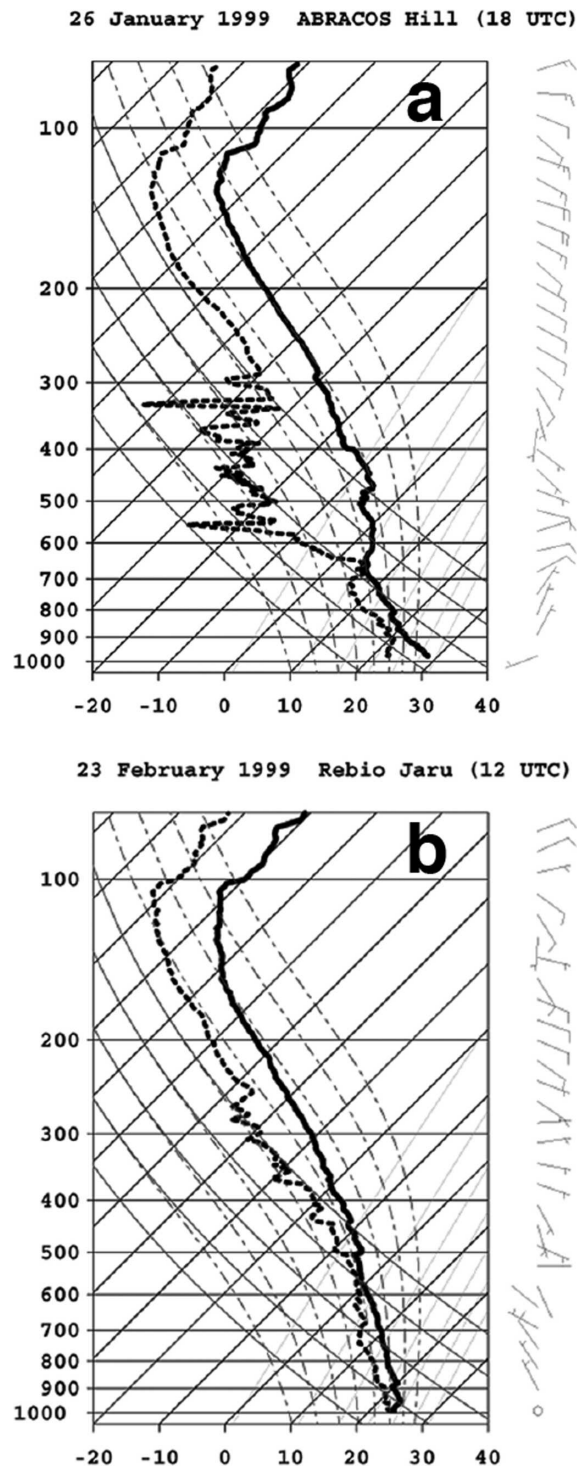


FIG. 2. Atmospheric environmental soundings for the (a) 26 Jan and (b) 23 Feb 1999 convective events. The 26 Jan thermodynamic profile comes from the 1800 UTC ABRACOS Hill sounding replaced with UVA tetheredsonde data below 890 mb. Temperature and relative humidity data from the Rebio Jaru sounding were used between 750 and 550 mb to remove cloud contamination. The 23 Feb profile was obtained from the 1200 UTC Rebio Jaru sounding. Full wind barbs denote 10 m s^{-1} , half-barbs 5 m s^{-1} .

al. (1998). The convection was widespread and rather weak—typical of that for the westerly regime, which has been described as being oceanic or monsoon-like (Cifelli et al. 2002; Rickenbach et al. 2002). Convection first began to form in the late morning around 1400 UTC (1000 LT) with the eruption of scattered, weak convective cells. By early afternoon, approximately 1700 UTC (1300 LT), convection had become widespread and was loosely organizing into southeast-northwest bands. A relatively long, thin line of convection developed by 2000 UTC but did not persist for long. It was in the process of decaying when the TRMM satellite made an overpass of it at 2100 UTC. Figure 1b shows a radar CAPPI along with dual-Doppler winds of the northern portion of this line at 2050 UTC near the time of the TRMM overpass. The CAPPI is at an altitude of 4 km. Peak convective core reflectivities are on the order of 40–45 dBZ. Soon after the time of this image, convection in the line died out, and by evening, 0000 UTC 24 February (2000 LT 23 February), convection across the TRMM LBA domain had completely dissipated.

3. Numerical model simulations

a. The Goddard Cumulus Ensemble model

The CRM used to perform the numerical experiments in this study is the 3D version of the GCE model. In the 3D version of the model, flow is fully compressible (Klemp and Wilhelmson 1978). A semi-implicit time-splitting scheme accommodates sound waves. Cloud microphysics includes a parameterized Kessler-type two-category liquid water scheme (cloud water and rain), and a Lin et al. (1983) or Rutledge and Hobbs (1984) three-category ice-phase scheme (cloud ice, snow, and hail/graupel). This study uses the Rutledge and Hobbs (1984) graupel ice physics. The sub-grid-scale turbulence (one-and-a-half order) scheme (Soong and Ogura 1980) accounts for the effects of condensation. The shortwave radiation parameterization of Chou and Suarez (1999) is used to compute solar heating, and the longwave radiation schemes of Chou and Kouvaris (1991), Chou et al. (1995, 1999), and Kratz et al. (1998) provide the infrared cooling. Cloud optical properties follow Sui et al. (1998) with the parameterization for cloud ice based on Fu and Liou (1993). Details of the cloud optical calculations are provided in Tao et al. (2003), and a review of CRM studies on cloud–radiation interaction can be found in Tao et al. (1996). Second- or higher-order accuracy advection schemes can introduce negative values of positive definite quantities (Soong and Ogura 1973). To alleviate this issue, a Multidimensional Positive Definite Advective

tion Transport Algorithm (MPDATA) was implemented into the model (Smolarkiewicz 1983, 1984) with a nonoscillatory option (Smolarkiewicz and Grabowski 1990). All scalar variables (potential temperature, water vapor, turbulent coefficient, and all five hydrometeor classes) use forward time differencing and the MPDATA for advection. The dynamic variables, u , v and w , use a second-order accurate advection scheme and leapfrog time integration (kinetic energy semiconserving method). Details of the model can be found in Tao and Simpson (1993) and Tao et al. (2003).

b. Setup, initialization, and numerical experiments

To accommodate the large, well-organized 26 January squall line, the model domain consisted of 152×166 grid points in the horizontal x and y directions, respectively, with 1.5-km resolution. This resolution is sufficient for simulating the key features of a squall line (Weisman et al. 1997). The lateral boundaries were open in the x direction and cyclic in the y direction. The outer portions of the grid were stretched along the x axis with a ratio of 1.05:1, resulting in a total grid length of 242.1 km. Grid spacing was constant in the y direction. A Galilean transformation or storm-relative reference frame was used to keep the system in the domain, effectively moving the model domain at a constant speed of 7.5 m s^{-1} to the west and 1 m s^{-1} to the south. A stretched vertical coordinate (height increments from 115 to 1165 m) with 31 levels was used to maximize resolution at low levels. The depth of the domain was 22.0 km. A sponge layer damped vertically propagating gravity waves above 15.5 km, and the model time step was 7.5 s.

The 26 January case was initialized using the 1800 UTC sounding launched from the Anglo-Brazilian Amazonian Climate Observation Study (ABRACOS) Hill site in the prestorm environment out ahead of the line. The lowest 1 km of thermodynamic data was missing from the sounding. This was filled in with tether-sonde data from the adjacent tether-sonde site, collocated at ABRACOS Hill. The original sounding also showed signs of cloud contamination at middle levels. This was corrected by replacing the temperature and relative humidity profiles between 750 and 550 mb with values from another sounding taken at Rebio Jaru at the same time. The final sounding, shown in Fig. 2a, shows weak boundary layer winds veering up to a midlevel easterly wind maximum of 10 m s^{-1} located near 600 mb. Winds are weak above the midlevel maximum but strengthen to 20 m s^{-1} easterlies near 150 mb. The 500-m mixed-layer CAPE for this sounding is 1632 J kg^{-1} , close to the 1500 J kg^{-1} reported by Halverson et al. (2002) for the mean easterly regime environment.

The final profile was interpolated to the model's vertical grid and applied horizontally uniform as the initial conditions. As squall lines are self-organizing, convection was initialized for this case by introducing a low-level cold pool into the model. The cold pool was 129 km long in the north-south direction, normal to the midlevel easterly wind maximum, 48 km wide and 4.9 km deep. The length was set to be similar to the observed system. A peak cooling rate of 0.00875 K s^{-1} was applied at the edge of the cold pool over the first 10 min of the simulation. Cloud growth was promoted on the upshear (left due to the moving reference frame) side by decreasing the cooling rate as a function of distance and height to the rear of the cold pool.

Three numerical experiments were performed for this case. The control run used the Rutledge and Hobbs (1984) graupel microphysics. Based on those results, two additional experiments were conducted that involved adjustments to the ice microphysics: run "dry0" and run "dry0sn-". In run dry0, the dry growth of graupel is turned off so that graupel particles do not accrete cloud ice or snow. Instead, the growth of graupel is restricted to riming and deposition processes. This was done in an effort to reduce the unrealistic presence of high-density ice in the anvil and stratiform portions of the cloud (Stith et al. 2002; Lang et al. 2004). In run dry0sn-, the collection efficiencies of cloud ice and cloud water by snow are reduced by an order of magnitude and by half, respectively, in addition to having no dry growth of graupel. Also, an alternate saturation scheme was used that yields far less cloud water and significantly more cloud ice above the freezing level (Tao et al. 2003), which is much more in line with in situ aircraft measurements of there being almost no supercooled cloud water in the anvil (Stith et al. 2002; Heymsfield et al. 2002). This run reduced excessive snow amounts in the anvil.

Convection on 23 February was widely scattered, weakly organized and slow moving. For this case, a model domain of 64 km by 64 km with constant grid resolution and cyclic lateral boundary conditions in both horizontal directions was used. The model reference frame was fixed. This setup allowed convective cells to slowly propagate through the domain. The vertical coordinate was again stretched using 41 levels (with height increments ranging from 37 to 1028 m) over a depth of 23 km. A sponge layer was again used in the top layers, and the model time step was 4 s. Convective initiation for this case required a different approach. Initial attempts at using a prestorm sounding with traditional cold pool or warm bubble initialization proved unsuccessful due to the lack of organizing shear. Initial convection was strongly determined by the initial

cold pool or warm bubbles then quickly died out. A different approach was therefore adopted. An early morning sounding was used instead, and convection was initiated by imposing time-varying surface fluxes into the model. This allowed convection to begin in a more realistic manner. The initial morning sounding for this case comes from the 1200 UTC sounding taken at Rebio Jaru (Fig. 2b). Low-level flow is weak and from the northwest. Winds aloft are also weak but reverse to easterlies. Relative humidities in this sounding are higher than in the 26 January profile. Combined with a 500-m mixed-layer CAPE of 934 J kg^{-1} , these attributes are well representative of the westerly regime environment presented in Halverson et al. (2002). The surface fluxes that were imposed into the model were based on data collected at two different sites: ABRACOS Hill and Ji Parana. Individual measurements from each site were used to construct simple diurnally varying sequences of sensible and latent heat fluxes whose peak amplitudes and overall diurnal signature matched those of the observations (Fig. 3). The Ji Parana-based fluxes were imposed in a 32 km by 32 km patch in the center of the domain surrounded by the ABRACOS Hill-based fluxes. The boundary between the two sets of fluxes provided the focus for convection. The fluxes were imposed into the model with no feedback from clouds or the atmosphere.

In addition to the same microphysics-based experiments that were conducted for the 26 January case, additional sets of experiments were made addressing the effects of horizontal grid resolution in the model. One set of runs used a horizontal spacing of 1000 m, similar to traditional values while the other used a much finer grid of 250 m. Maintaining the physical size of the domain at 64 km by 64 km for both sets of runs required 64 by 64 and 256 by 256 horizontal grid points, respectively. The 3D GCE model was used with a similar setup to participate in a model comparison study by Grabowski et al. (2006), which adopted this same case to study diurnal convective development over land. The same sounding and ABRACOS Hill-based fluxes were prescribed in that study only the ABRACOS Hill-based fluxes were applied over the entire domain.

4. Results and analysis

a. Overall patterns

The overall pattern obtained from each of the numerical experiments for both cases (for brevity, only the control run results are shown from the 1000-m 23 February runs) can be seen in Fig. 4, which shows the simulated radar reflectivities at a height of 4 km, the same as the observed CAPPIS shown in Fig. 1. In gen-

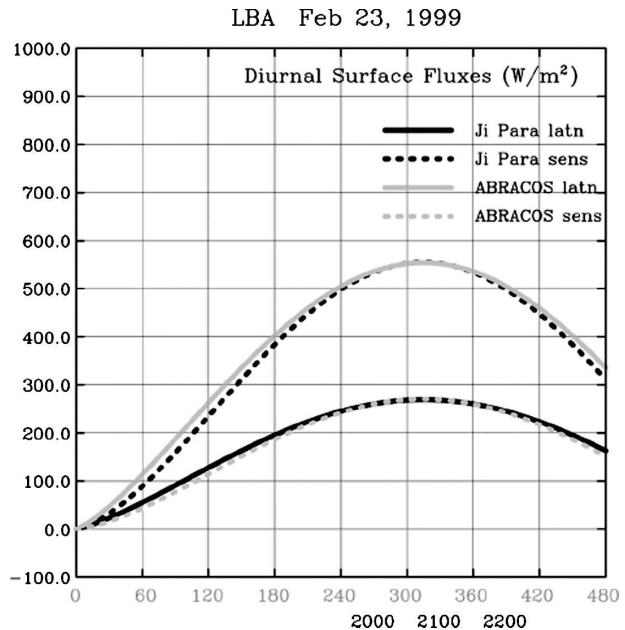


FIG. 3. Imposed diurnal surface latent and sensible heat fluxes used for convective initiation in the 23 Feb 1999 simulations. The values are based on surface flux data collected from ABRACOS Hill and Ji Parana.

eral, the model accurately captures the convective organization in each case. All of the 26 January runs result in a squall line with a generally north-south-oriented leading convective band, normal to the low-level shear and midlevel wind maximum, with a trailing stratiform region. Core reflectivities exceed 50 dBZ at this level, similar to those from the observations shown in Fig. 1. Differences in the trailing echo between the control run and runs dry0 and dry0sn- are apparent with runs dry0 and dry0sn- having broader areas of moderate intensity echo (i.e., between 20 and 40 dBZ). This is a key difference between the control run and the observations. The control run lacks the broad area of moderate echo visible in the observations. Other factors, such as the model domain size or midtropospheric moistening from previous convection that cannot be accounted for, could also impact the physical size of the simulated precipitation area, but these would effect all of the simulations and not just the control. Simulated radar reflectivities were calculated from the model hydrometeor contents based on the formulation of Smith et al. (1975) and Smith (1984).

For the 23 February simulations, the model produces loosely organized convective lines that are oriented south-southeast to north-northwest, parallel to the deep tropospheric shear vector and in good agreement with the observed organization. Newer convection occurs on the eastern side of the line with a small area of

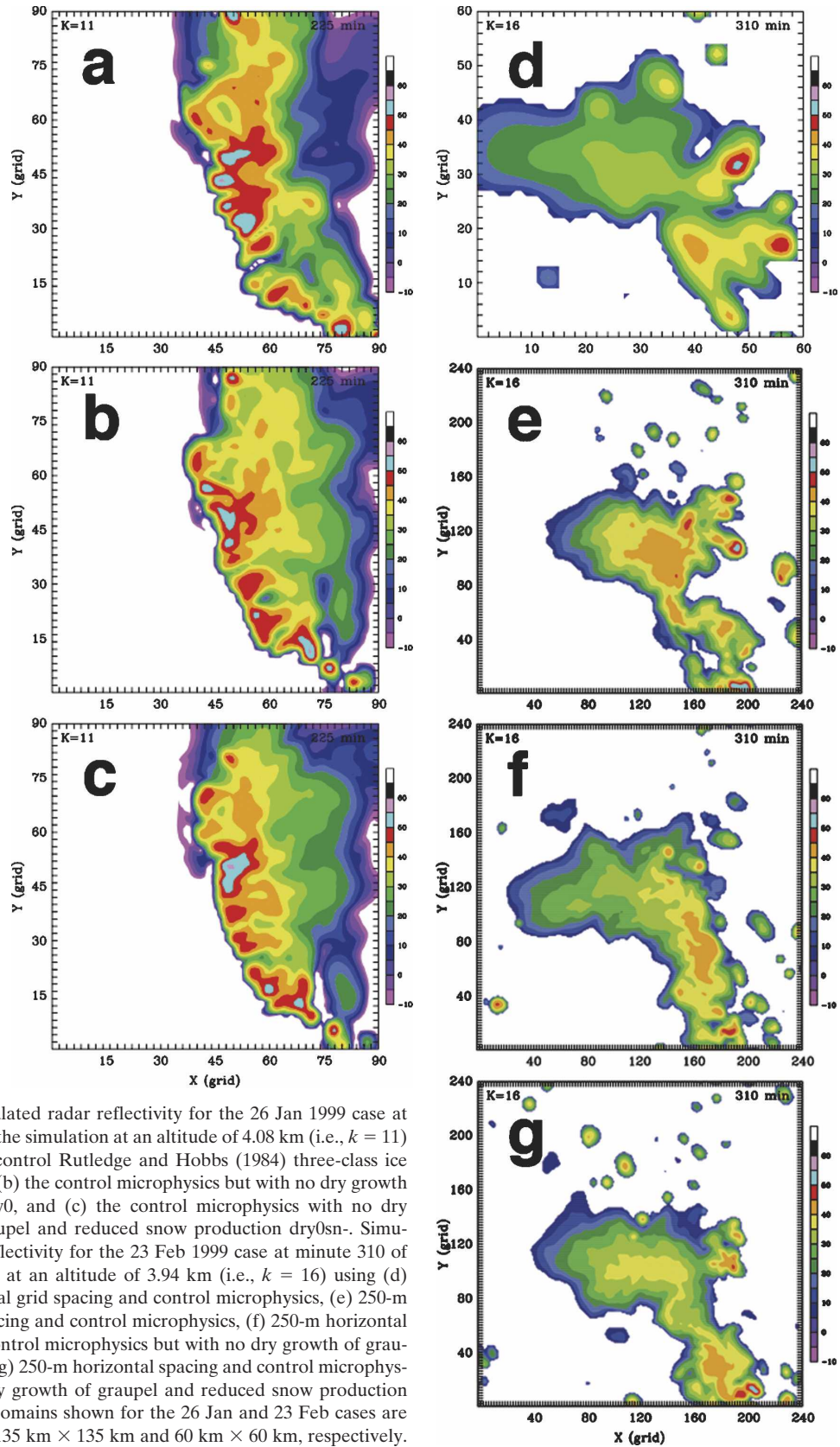


FIG. 4. Simulated radar reflectivity for the 26 Jan 1999 case at minute 225 of the simulation at an altitude of 4.08 km (i.e., $k = 11$) using (a) the control Rutledge and Hobbs (1984) three-class ice microphysics, (b) the control microphysics but with no dry growth of graupel $dry0$, and (c) the control microphysics with no dry growth of graupel and reduced snow production $dry0sn-$. Simulated radar reflectivity for the 23 Feb 1999 case at minute 310 of the simulation at an altitude of 3.94 km (i.e., $k = 16$) using (d) 1-km horizontal grid spacing and control microphysics, (e) 250-m horizontal spacing and control microphysics, (f) 250-m horizontal spacing and control microphysics but with no dry growth of graupel $dry0$, and (g) 250-m horizontal spacing and control microphysics with no dry growth of graupel and reduced snow production $dry0sn-$. The domains shown for the 26 Jan and 23 Feb cases are equivalent to 135 km \times 135 km and 60 km \times 60 km, respectively.

stratiform trailing off to the north and west, which also agrees well with the observed line of convection. Simulated core reflectivities are slightly more intense than was observed. This will be analyzed in more detail in the following sections.

b. Diurnal growth

A well-known problem with large-scale models is their inability to accurately capture the phase of the diurnal cycle of convection, especially over land (Bechtold et al. 2004; Betts and Jakob 2002; Guichard et al. 2004; Yang and Slingo 2001) with deep convection characteristically occurring abruptly and too early in the model by several hours. One of the objectives of the GCSS is to use CRMs to help improve large-scale models. However, the horizontal resolutions used in CRMs to simulate deep convection (i.e., typically 1 km or coarser) are often too coarse themselves to allow the models to resolve this issue (Petch et al. 2002). The objective of the Grabowski et al. (2006) study was to investigate the growth phase of the diurnal cycle, from the formation of shallow convection after sunrise through the transition to deep precipitating convection, using CRMs and single-column models (SCMs). The GCE model results reported in that study showed that using a finer resolution (250 m versus 1000 m) resulted in a smoother transition to deep convection. Similar results are obtained in this study, which uses diurnally varying surface fluxes from two sites, as opposed to the single site used in the Grabowski et al. (2006) study.

Figure 5 shows time–height cross sections of maximum vertical velocities and equivalent radar reflectivities using both 1000-m and 250-m resolution. In the 1000-m run, convection intensifies quickly with maximum vertical velocities increasing from 0.5 to over 25 m s⁻¹ in just 80 min (Fig. 5a). In contrast, a much longer and more gradual intensification period of 200 min is achieved using 250-m horizontal resolution (Fig. 5b). A similar trend is also evident in the maximum reflectivities. Echo top heights rapidly increase from about 3 to 16 km over a span of just 40 min in the 1000-m run (Fig. 5c). This behavior mimics the problem with larger-scale models wherein convection becomes deep almost immediately. On the other hand, the transition from shallow convection with echo tops near 2 km to deep convection with echo tops over 16 km takes almost 2 h in the 250-m run (Fig. 5d). The peak vertical velocities and reflectivities are actually quite similar between the two resolutions; however, convective intensity in the 250 m simulation is steadier as opposed to being more pulse-like in the 1000-m run as evidenced by the more isolated protrusions of 40-dBZ echo well above the freezing level in that run.

The overall convective characteristics in these two runs and the differences between them are consistent with the ability of the finer resolution model to resolve smaller-scale circulations. As shown by Grabowski et al. (2006), mean cloud widths occur initially at the horizontal resolution of the model. Furthermore, the mean cloud widths in the 250-m resolution simulation remained smaller than what could be resolved in the 1000-m simulation. This has a direct impact on cloud entrainment. Saturated updrafts cannot occur at finer scales. This results in the coarser model producing fewer, more undilute convective cores that ascend higher into the troposphere. In effect, the coarser resolution model is inherently limited in its ability to produce shallow convection and congestus-type clouds. These characteristics are less desirable and more unrealistic than what was obtained using the finer 250-m resolution. This suggests the horizontal resolutions normally used to simulate deep convection are inadequate for the diurnal growth of convection in this type of environment and that finer resolutions are needed.

c. Comparisons with radar observations

Dual-Doppler radar observations were collected on both 26 January and 23 February by the NASA TOGA and NCAR S-Pol radars. Cifelli et al. (2002) completed dual-Doppler analyses for two cases, including 26 January. Results from that analysis along with a similar analysis for 23 February will be used to evaluate the model simulations. The model and radar data will be compared using a statistical technique developed by Yuter and Houze (1995), namely contoured frequency with altitude diagrams (CFADs). This technique computes the probability density of a field as a function of height. To achieve the most meaningful comparisons, the CFADs must be computed as similarly as possible between the model and radar-derived fields, and an appropriate period from the model must be selected to compare with the observations.

To construct the CFADs between the observed and model data as similarly as possible, the same number of bins and bin sizes used to compute the radar CFADs were used to compute the model CFADs. The resolution of the model data was also matched to that of the radar grid when possible. All of the dual-Doppler analyses were performed on a 1-km horizontal grid. This matches the 1000-m 23 February run so no adjustment was made to that model data. Data from the 250-m 23 February runs were averaged over 1 km before performing any analyses. Data from the 26 January runs could not be made to fit the 1 km radar grid and were left at 1.5 km, resulting in a slight difference in the resolution of the modeled and observed analyses for

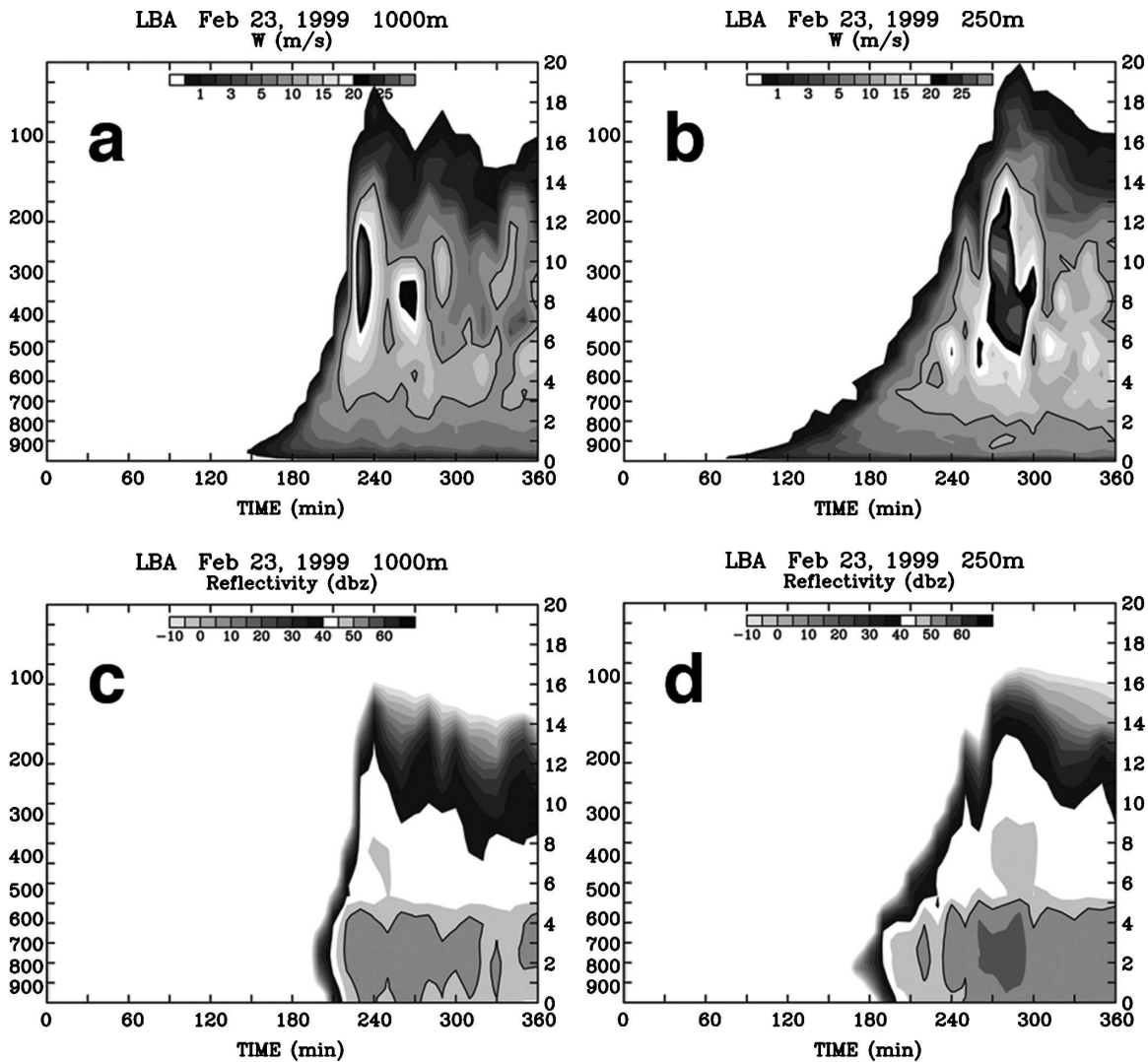


FIG. 5. Time–height cross sections obtained from the 23 Feb 1999 simulations of maximum (a) vertical velocity using 1-km horizontal grid spacing, (b) vertical velocity using 250-m horizontal spacing, (c) reflectivity using 1-km horizontal spacing, and (d) reflectivity using 250-m horizontal spacing.

26 January. The final requirement is to match up the time of the radar analysis with an appropriate period from the model. Currently, the objective of CRM simulations is to represent accurately the observed storm characteristics statistically and not the exact time of occurrence of a particular convective cell. Consequently, the stage of the simulated convection was matched with that of the observed convection by comparing their convective fractions. This was accomplished by applying the same convective–stratiform separation technique used in the radar analyses, based on Rickenbach and Rutledge (1998) and Steiner et al. (1995), to the model data. Figure 6 shows the modeled and observed convective fractions for both the 26 January and 23 February cases. Based on the observed con-

vective fractions for 26 January, the simulation time from minute 210 to 360 was identified as the most representative of the observation period. The convective fractions indicate that during this period the system went from its mature to its dissipating stage. For 23 February, the period from minute 300 to 360 provides the closest match. The model convective fractions are higher than observed, and unlike 26 January, they remain high throughout the simulation. This may be a result of imposing the surface fluxes and might be improved with an interactive land surface model. Also, after minute 360 in the 23 February simulations, new convection broke out across the domain as a result of outflows propagating back through the cyclic boundaries. This period was thus eliminated from analysis.

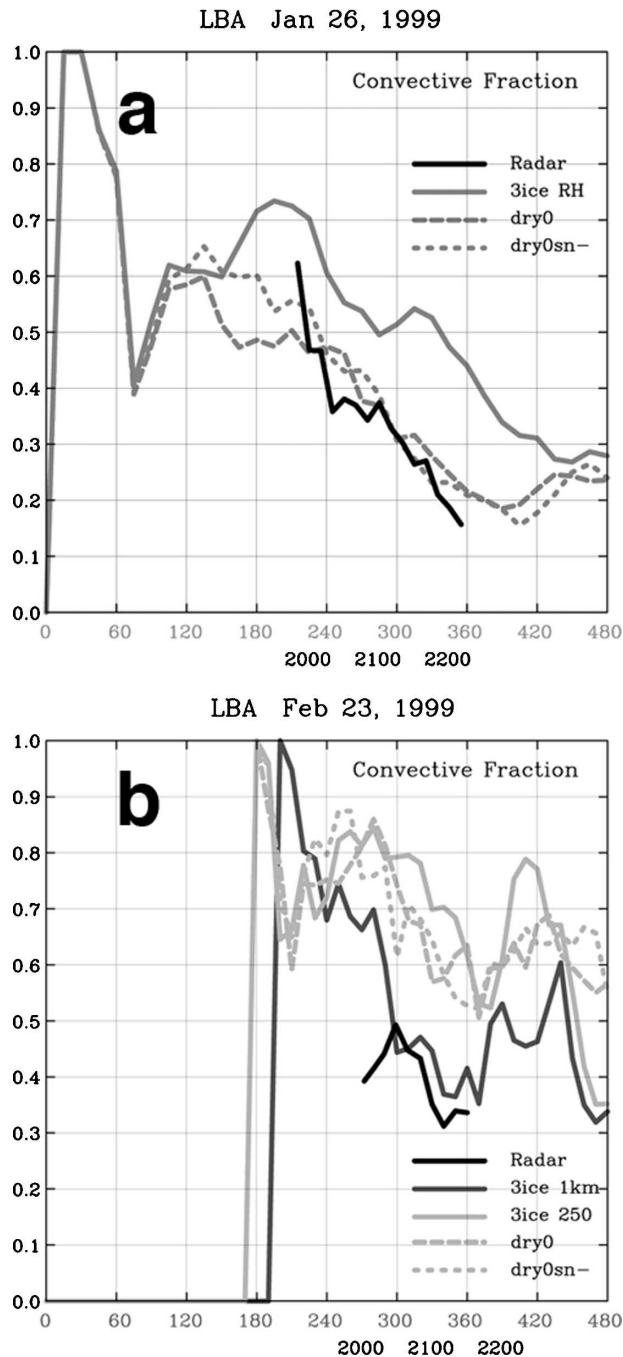


FIG. 6. Simulated and observed convective fractions based on the Steiner et al. (1995) convective–stratiform separation technique for the (a) 26 Jan and (b) 23 Feb 1999 cases.

Figure 6a shows the convective fractions for the 26 January control run to be systematically higher than runs dry0 and dry0sn-. The reason for this is illustrated by the simulated radar x - y cross sections shown in Fig. 4. The control run contains a broader area of 40-dBZ echo relative to the moderate echo area. This 40-dBZ

echo will be identified as convective by the separation algorithm. Lang et al. (2003) compared a variety of separation algorithms using model simulations. They concluded that significant quantitative differences between the algorithms could be due to unrealistic aspects of the model simulations rather than problems with the algorithms. It was felt that more realistic model simulations might allow the algorithms to converge. One of the unrealistic aspects of the model simulations was the presence of high-density ice throughout the anvil (Lang et al. 2004). This high-density ice contributes to the broad 40-dBZ echo in the control run. Eliminating the high-density ice outside the convective cores results in a more realistic simulation and seems to improve the performance of the separation algorithm as evidenced here for the 26 January case. This effect is not very noticeable for 23 February due to the lack of a large, organized stratiform area.

1) REFLECTIVITY CFADS

Reflectivity CFADs were constructed by binning the reflectivities into 2-dBZ bins beginning at -10 dBZ at each level. Figure 7a shows the observed CFAD for 26 January. The highest probabilities follow a coherent pattern with the peak density steadily decreasing with height from between 20 and 35 dBZ near the melting level to between 5 and 15 dBZ near storm top around 17 km. Below the melting level, there is evidence of evaporation as peak probabilities gradually decrease toward the surface. Maximum reflectivities are just over 55 dBZ between 4 and 7 km, around 55 dBZ at the surface, and drop off steadily aloft. The control run CFAD, shown in Fig. 7b, has several notable differences. Peak probabilities are disjointed above and below the melting level, and are shifted too high near the surface, between 30 and 40 dBZ, and too low aloft. The low-level distribution also shows no evidence of evaporation. At low levels, maximum simulated reflectivities are only slightly higher than observed. However, low-level 50 dBZ echoes occur at a frequency of 2% in the model but were observed to occur at a frequency of just 0.1%. Above the freezing level, peak simulated reflectivities are more intense than was observed. Furthermore, reflectivities of 35 dBZ or more occur far too frequently in the model compared to the radar observations.

Reflectivity calculations revealed that the shift to higher reflectivities aloft was due to graupel. As noted by Lang et al. (2004), the problem with graupel (or hail) in a one-moment bulk microphysical scheme is that once carried aloft into the anvil it tends to remain. This results from sedimentation being the only real sink

term for graupel above the freezing level. Also, a one-moment scheme treats small amounts of graupel not as a few large particles but as many smaller particles, further extending its lifetime in the anvil. Once in the anvil, graupel continues to grow through accretion processes. This situation provided the impetus for run dry0 wherein graupel is restricted from accreting cloud ice and snow. The basis for this is twofold. One is to mitigate the improper presence of high-density ice in the anvil as aircraft data support bulk densities for precipitation-sized particles that are far less than the 0.4 g cm^{-3} used for graupel (Heymsfield et al. 2002). The other, which makes this solution plausible, is that graupel is a product of riming. A small graupel particle that collides with cloud ice or snow (i.e., ice crystals or aggregates) should not become a larger high-density ice particle. The CFAD for run dry0 (Fig. 7c) shows some key improvements over the control run. The biggest improvement is the overall shift in frequencies toward the observed values. This is especially true below the melting level where the maximum echo occurrence is now between 20 and 35 dBZ, very close to the radar. However, model evaporation is now very pronounced. In run dry0, anvil rain originates from melting snow rather than melting graupel as much of the graupel is replaced by snow [see section 4d(1)]. Slower-falling snow particles remain suspended longer than graupel and are advected farther from the convective cores. This explains the broader stratiform area in run dry0. The end result is smaller rain rates spread over a wider area, which leads to more evaporation. A compounding effect is that rain evaporation is already too strong in a one-moment scheme as it cannot include the effects of size-separation and results in too many smaller drops. This effect also appears in the rainfall histograms [section 4c(3)]. Maximum reflectivities in run dry0 are almost unchanged from the control and remain higher than observed.

Despite the notable gains of run dry0, the probability of echoes greater than 25 dBZ above 8 km is still noticeably higher than was observed. The higher likelihood of model echoes in this range is due to unrealistically large amounts of snow. Aircraft data show that except near the melting layer particle size distributions in the anvil are dominated by small particles not aggregates (Heymsfield et al. 2002). Several approaches were tried to reduce the snow amounts. First, an alternate saturation scheme was tried that results in more cloud ice and less cloud water in the anvil (Tao et al. 2003). This had almost no impact on the excessive snow, however. So, in addition, the collection efficiency of cloud ice by snow was reduced from 0.1 to 0.01, but snow

amounts remained high although cloud ice was modestly increased near cloud top. Hong et al. (2004) recommended using a temperature-dependent collection efficiency for cloud ice, which is physically reasonable; however, their range of values is generally higher than the values tested here. The dominant source term for snow is snow accretion of cloud water (Lin et al. 1983). It was therefore decided to also reduce the collection efficiency of this term from 1.0 to 0.5, which finally reduced the snow contents and is termed run dry0sn-. CFAD results from this run (Fig. 7d) show further improvement in the reflectivity distributions aloft. The probability of echoes greater than 25 dBZ above 8 km is reduced. And, the overall distribution further converges into a coherent core of higher probabilities, closer to the radar distribution. An indirect benefit of the broader anvils in dry0 and dry0sn- is that the relative probability of weak echo (i.e., less than 10 dBZ) on the periphery of the echo region is reduced. This improves the overall agreement with the radar data as is apparent in the dry0sn- CFAD. The high frequency of echoes less than 0 dBZ, so prominent in the control run, is reduced. Peak reflectivities in dry0sn- remain similar to both the control and dry0, exceeding the radar values. This persistent feature is due to core reflectivities being too intense and could be yet another artifact of size separation. Excessive evaporation at low levels is further exaggerated in run dry0sn-.

Results for 23 February are shown in Figs. 7e-i. Compared to the 26 January squall line, the observed reflectivity CFAD for 23 February (Fig. 7e) shows a significant shift at middle and low levels to weaker values. This results in a distribution wherein the maximum probabilities change very little with height. Reduced low-level evaporation and a less prominent bright band are consistent with the lack of a large, coherent stratiform region. The moister environment also serves to limit evaporation. Although the overall storm height is less on 23 February, maximum reflectivities are fairly similar. Results from the 1000-m simulation are shown in Fig. 7f. Peak densities at low levels are shifted too high, between 15 and 30 dBZ, as opposed to the 5 to 15 dBZ range of the radar. Despite evaporation being much weaker than for 26 January, there is still evidence of weak evaporation in the radar data that the model omits. Maximum simulated reflectivities agree well with the radar at low levels but are too high aloft. Finally, the core of highest probabilities decreases sharply with height in the simulation, which was not observed, and the overall storm height is lower than for the radar. Figure 7g shows the 250-m resolution results using control microphysics. At all but the very top levels, maxi-

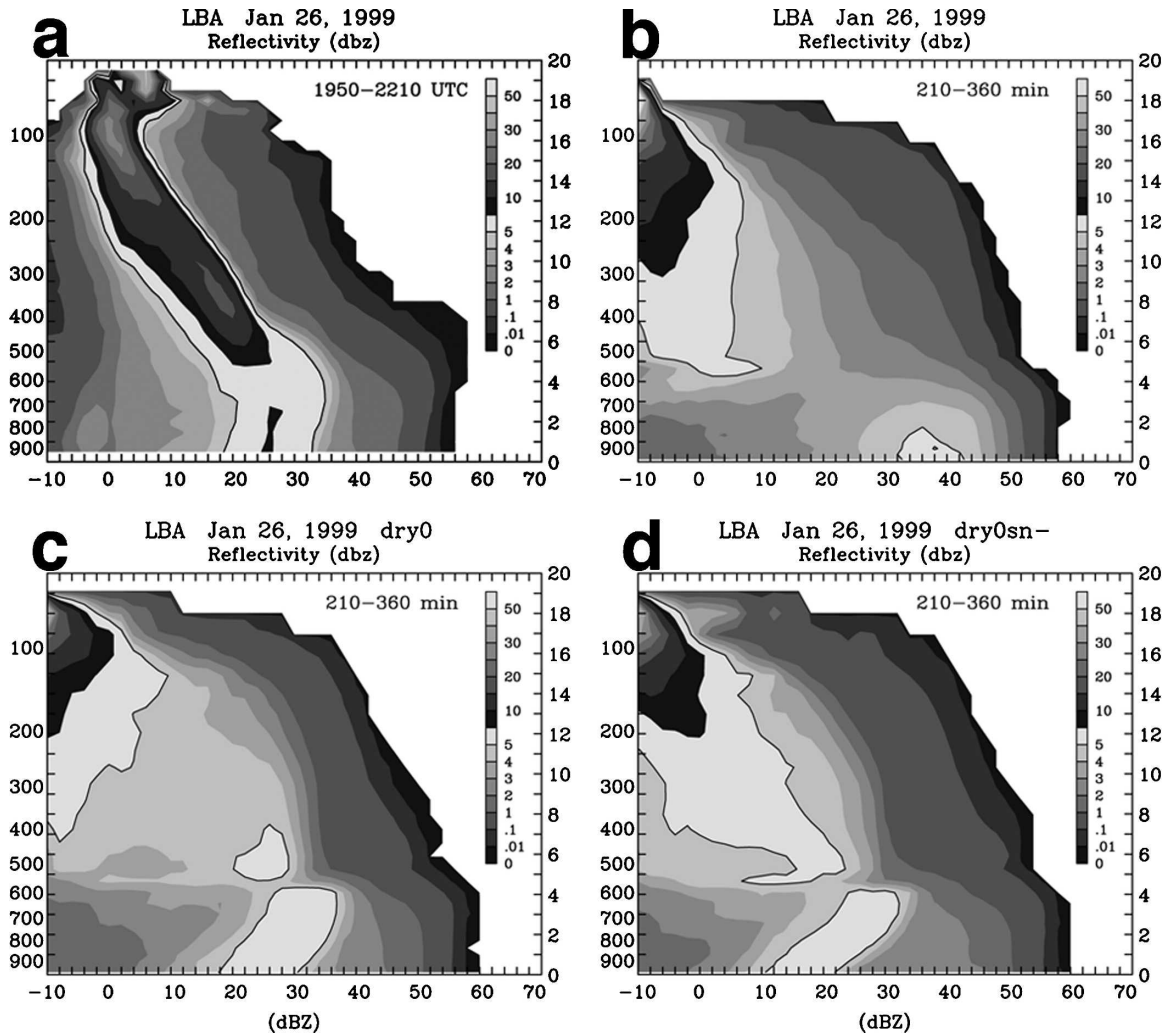


FIG. 7. Reflectivity CFADs for the 26 Jan 1999 case derived from (a) observed S-pol radar reflectivity data, (b) the simulation using control microphysics, (c) the simulation using control microphysics but no dry growth of graupel dry0, and (d) the simulation using control microphysics with no dry growth of graupel and reduced snow production dry0sn-. Reflectivity CFADs for the 23 Feb 1999 case derived from (e) observed S-pol radar reflectivity data, the simulation using (f) 1-km horizontal grid spacing and control microphysics, (g) 250-m horizontal spacing and control microphysics, (h) 250-m horizontal spacing and control microphysics but no dry growth of graupel dry0, and (i) 250-m horizontal spacing and control microphysics with no dry growth of graupel and reduced snow production dry0sn-.

mum reflectivities are the same as in the 1000-m run. At low levels, the core of high probabilities is slightly less peaked and centered at slightly higher values in the 250-m run. Above the freezing level, the 250-m distribution is shifted to higher values, in worse agreement with the radar, but the storm top is higher in better agreement with the radar. This is due to the timing of deep convection (see Figs. 5c,d). In the 1000-m run, the analysis period falls in between the time of the deepest convection, while in the 250-m run there is less undulation in the overall convective intensity at any given time.

The dry0 and dry0sn- 250-m resolution CFADs are shown in Figs. 7h and 7i, respectively. As the 23 Feb-

ruary case does not have a large, coherent anvil, the effect of the modified microphysics is somewhat lessened as there is less area for some of the ice interactions to occur. However, the frequency of echoes that are too high aloft (e.g., the probability of echoes over 35 dBZ above the freezing level) is reduced. The modified physics also tends to produce more echoes in the 10- to 30-dBZ range above the freezing level. Maximum reflectivities in the three 250-m runs are nearly the same at all levels. With the overall echo pattern more convective than was observed (Fig. 6b), further improvement may require more realistic surface forcing via the use of an interactive land surface model.

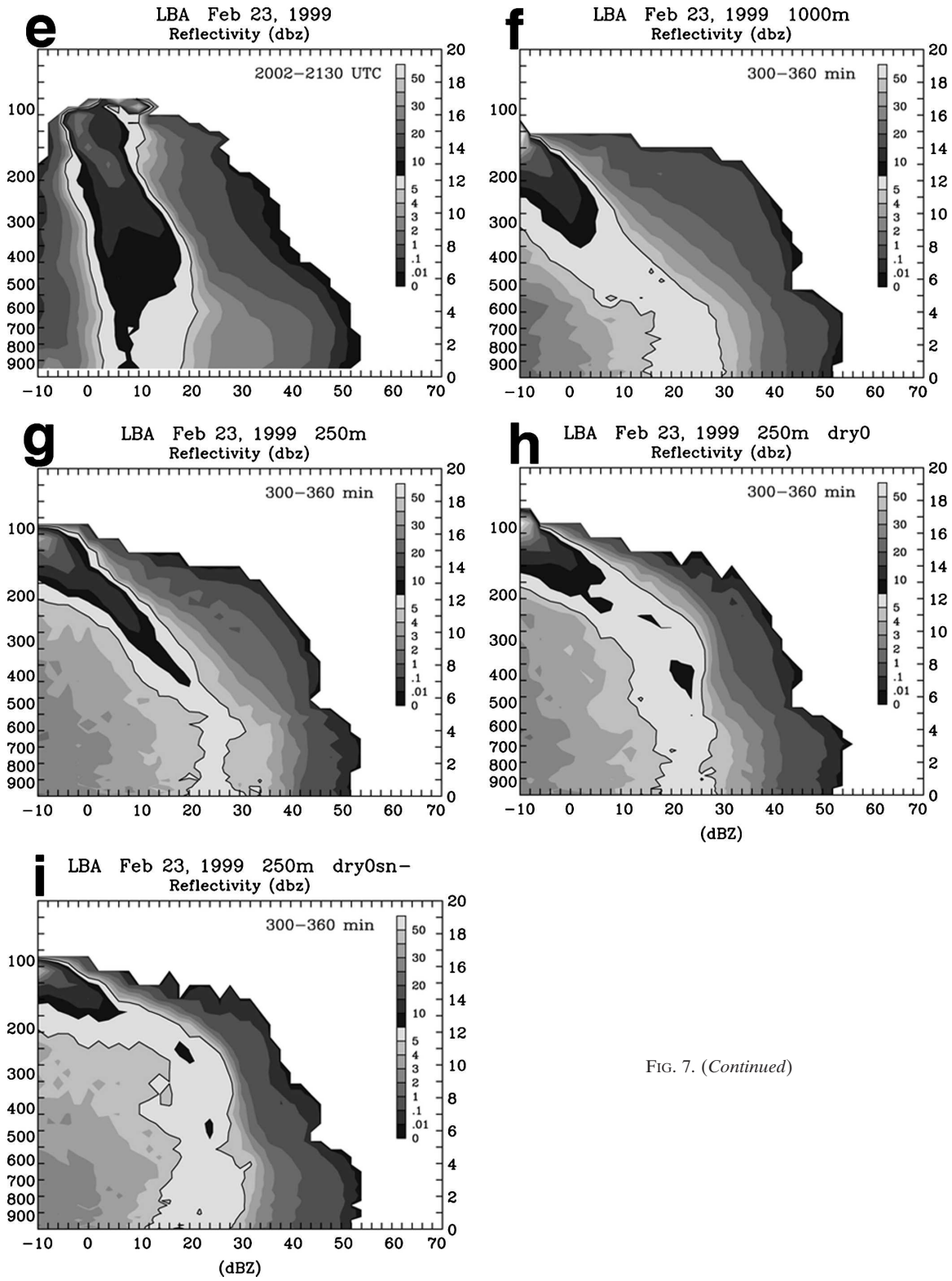


FIG. 7. (Continued)

2) VERTICAL VELOCITY CFADS

In addition to reflectivities, CFADs of vertical velocities were constructed by binning either dual-Doppler derived or model-simulated cloud drafts into 1 m s^{-1} bins beginning at -15 m s^{-1} at each level. Figure 8a shows a vertical velocity CFAD constructed from dual-Doppler syntheses for 26 January. The syntheses were made using a downward integration technique with the lowest level at 0.5 km AGL (see Cifelli et al. 2002). Maximum updrafts are on the order of 30 m s^{-1} at upper and lower levels, and 10 m s^{-1} updrafts occur at a frequency of 0.1% at all levels. Downdrafts exceed 15 m s^{-1} at most levels, and the probability of downdrafts of between 6 and 8 m s^{-1} is about 0.1% throughout the depth of the storm. Model-simulated drafts (Fig. 8b) agree quite well with the Doppler analyses at upper levels, especially for updrafts. At lower levels, however, both the model updrafts and especially the downdrafts are considerably weaker than those from the dual-Doppler analyses. The fact that strong updrafts and downdrafts are present near the surface in the Doppler analyses and that a downward integration was adopted, which results in divergence errors accumulating toward the surface, means that the lower levels of the radar vertical velocity CFAD are suspect. Still, the overall intensity of convection in the model is reasonably close to that observed as evidenced by the similarity in peak updrafts and probability of 10 m s^{-1} updrafts. Results from runs dry0 and dry0sn- (not shown) are very similar to Fig. 8b.

For 23 February (Fig. 8c), the maximum Doppler-derived updrafts are significantly weaker, although they reach 20 m s^{-1} at midlevels. Peak downdrafts are also considerably weaker than on 26 January. However, the distribution of drafts between 5 and 10 m s^{-1} is remarkably similar as evidenced by the fairly identical position of the 0.1% probability contour for both cases. Because downward integration was used here also, the accuracy of the distribution at low levels is questionable although the results do not appear as egregious as with 26 January. Results from the 1000-m simulation (Fig. 8d) indicate model convection is slightly weaker than was observed by the radar, having peak updrafts of just 15 m s^{-1} and a probability of 10 m s^{-1} updrafts less than 0.1%. The CFAD from the 250-m simulation (Fig. 8e) closely resembles the 1000-m run but with a higher storm top. The overall structure and intensity of runs dry0 and dry0sn- (not shown) mimic that of the base 250-m run.

3) RAINFALL HISTOGRAMS

Rainfall histograms were constructed for both cases over the same analysis periods using a bin size of

5 mm h^{-1} beginning at 0 mm h^{-1} . Details on the derivation of rain rates from the radar can be found in Cifelli et al. (2002). The 26 January histograms from the radar and all three model runs are shown in Fig. 9a. The dry0 and dry0sn- histograms have the same characteristic shift towards lower frequencies across the entire distribution above 5 mm h^{-1} . This shift coincides with a shift in the origin of anvil rain from melting graupel to melting snow and with the increase in evaporation below the melting level. The base and modified microphysics histograms bracket the radar distribution at moderate rain intensities between 10 and 50 mm h^{-1} . The model, however, characteristically underestimates the occurrence of high rain rates. This underestimation is consistent with the inability of a one-moment microphysics scheme to allow size sorting of precipitation particles and to overestimate evaporation.

The 23 February results (Fig. 9b) are analogous to the reflectivity CFADs where the modifications in runs dry0 and dry0sn- have minimal impact due to the overabundance of convective area and result in little variation between the model histograms. The same problem with the one-moment scheme is also depicted here with the model being unable to reproduce the more intense rain rates. However up to about 20 mm h^{-1} , which constitutes the bulk of the occurrences, the model histograms match well with the observed values. The real discrepancy with the radar is in the tail of the distribution.

d. Comparisons with satellite radiometer observations

In addition to ground-based radar, microwave radiance observations were collected on the 23 February convective system from the TRMM Microwave Imager (TMI) during an overpass at 2100 UTC. Over land, TMI radiances at 37 and 85.5 GHz are mostly sensitive to scattering by ice-phase precipitation particles (graupel and snow), which scatter upwelling thermal microwave emission and lower the observed brightness temperatures. Depressions in observed brightness temperatures relative to a reference temperature of 273 K were compared to simulated brightness temperature depressions derived from the 23 February simulations at minute 310, approximately the same stage of development as the observed system. (A brightness temperature of 273 K would represent a thick cloud or rain layer extending vertically up to the freezing level; thus, brightness temperatures lower than 273 K indicate scattering by precipitation-sized ice.) The simulated upwelling brightness temperatures at the resolution of the model were calculated using Eddington's second approximation (see Olson et al. 2001). The resolution of

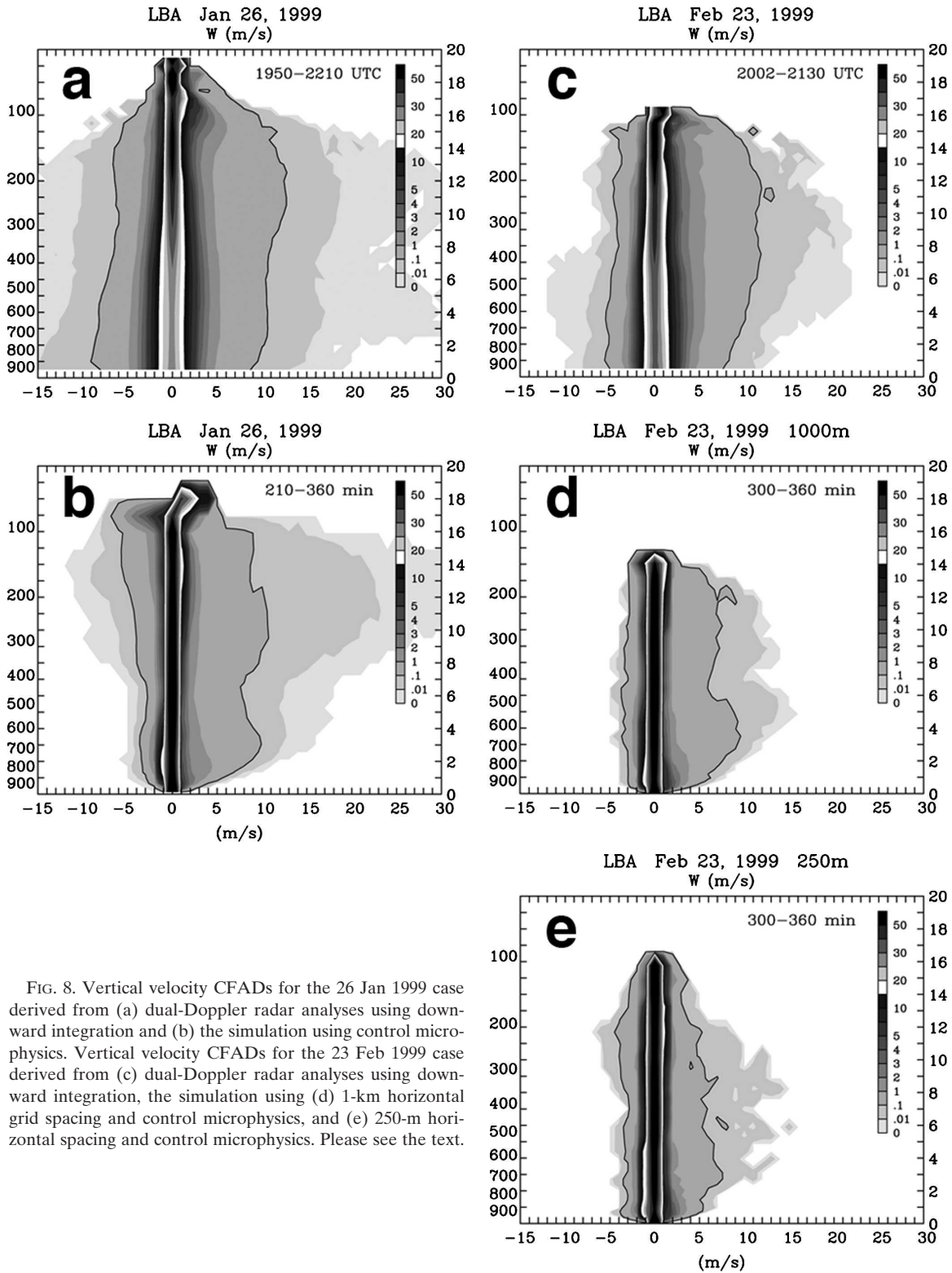


FIG. 8. Vertical velocity CFADs for the 26 Jan 1999 case derived from (a) dual-Doppler radar analyses using downward integration and (b) the simulation using control microphysics. Vertical velocity CFADs for the 23 Feb 1999 case derived from (c) dual-Doppler radar analyses using downward integration, the simulation using (d) 1-km horizontal grid spacing and control microphysics, and (e) 250-m horizontal spacing and control microphysics. Please see the text.

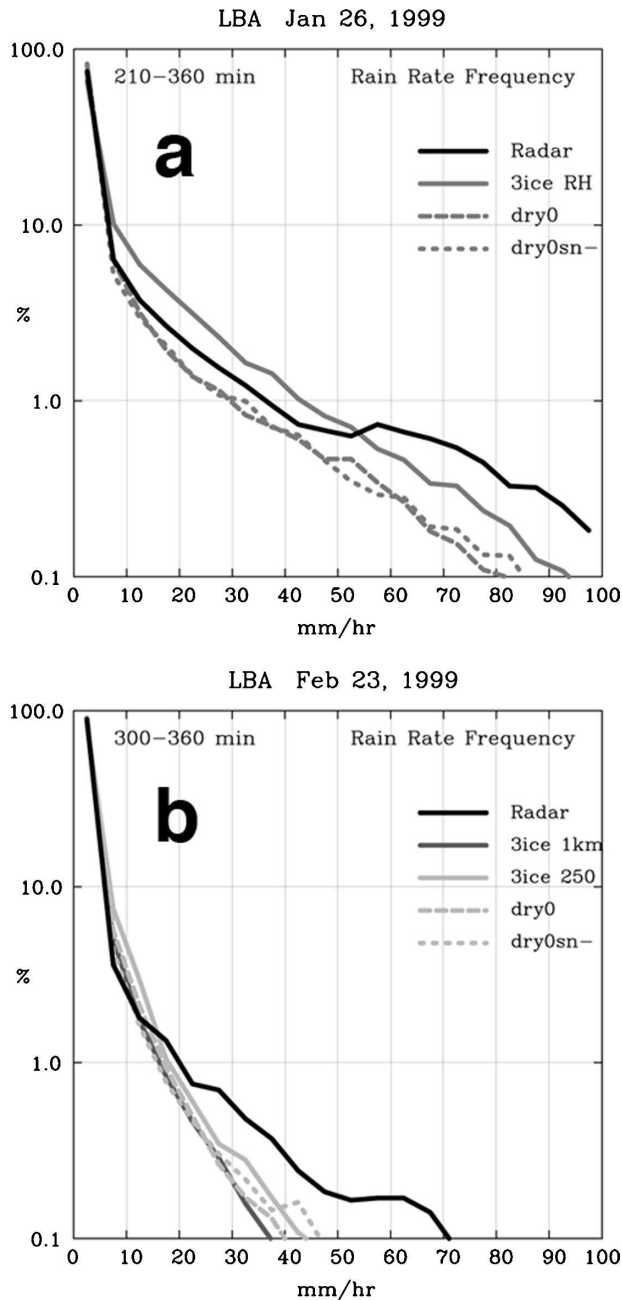


FIG. 9. Radar-derived and model-simulated rainfall histograms for the (a) 26 Jan and (b) 23 Feb 1999 cases.

the TMI was simulated by convolving the model-resolution radiances using 2D Gaussian functions to approximate the diffraction limitation of the microwave observations, and by sampling the convolved radiances at the spacing of the TMI all-channel footprints. As the real convective system was somewhat larger than the simulated system, the mean scattering depressions at 37 and 85.5 GHz and number of footprints with a scatter-

TABLE 1. Simulated and observed mean scattering depressions at 37 GHz (S37) and 85.5 GHz (S85) and number of footprints with positive scattering depressions corresponding to the 2100 UTC TMI overpass of the 23 February convective system.

	Mean S37/ No. of footprints	Mean S85/ No. of footprints
250-m base	24.9/9	68.5/10
250-m dry0	16.9/8	48.6/10
250-m dry0sn-	13.5/7	51.1/9
TMI observed	6.1/12	26.0/53

ing depression greater than zero are used for comparison.

Table 1 lists the scattering depression statistics for the three 250-m-resolution model runs and the TMI observations. The base microphysics results in mean scattering depressions at 37 and 85 GHz that exceed the observed depressions by factors of roughly 3–4. However, the number of simulated footprints with significant scattering depressions at 85.5 GHz is significantly less than the number observed. This suggests that the model generates a more compact, intense system with more precipitation ice than the actual system. The dry0 and dry0sn- simulations reduce the mean scattering, bringing it closer to the observed, but the area of the scattering region is also slightly reduced.

e. Hydrometeor profiles

Domain-average profiles of hydrometeor content were made for each of the model simulations. The 26 January results were averaged over the first 480 min of simulation time (Figs. 10a–c). Figure 10a shows the dominant form of ice using the base Rutledge and Hobbs (1984) ice microphysics is graupel with much smaller amounts of snow and cloud ice. Eliminating the dry growth of graupel results in a significant reduction in graupel and an enormous increase in snow (Fig. 10b). This shift in the dominant form of precipitation ice from higher-density rimed graupel to aggregates (i.e., snow), especially in the anvil, qualitatively agrees much better with observations (Stith et al. 2002). However, based on the reflectivity CFAD comparisons with the radar data and in situ measurements of particle size distributions (Heymsfield et al. 2002), these snow contents are too high. The abundant snow in run dry0 reduces the already small amount of cloud ice aloft. Average rain and cloud water contents below the melting level, however, are unaffected, although the increase in evaporation in run dry0 is apparent in the increased slope of the rain content toward the surface. In run dry0sn- (Fig. 10c), snow contents are significantly reduced from run dry0 but are still much larger than in

the control run. Graupel is slightly higher, and cloud ice increases significantly and accounts for a significant fraction of the ice in the upper portion of the cloud, resulting in a much more realistic profile when compared to in situ aircraft data wherein smaller cloud ice-sized particles dominate the particle size distribution in the upper portions of the anvil while aggregates (or snow) dominate closer to the melting layer (Heymsfield et al. 2002). The key to reducing the snow was to decrease the collection efficiency of cloud water by snow from 1.0 to 0.5. Changing the collection efficiency of cloud ice by snow from 0.1 to 0.01 had little effect on the snow mass and only slightly increased the cloud-ice content (not show). Likewise, switching saturation schemes had almost no effect on snow amount. The rain and cloud water profiles in run dry0sn- are unchanged from run dry0.

Average hydrometeor profiles for 23 February over the first 360 min of simulation time are shown in Figs. 10d–g. As with the CFADs and rainfall histograms, the 23 February results are dominated by the convective region. The 1000- and 250-m results, Figs. 10d and 10e, respectively, are very similar with the only real difference being a slight increase in the cloud water amount in the 250-m run. Both simulations are completely dominated by graupel aloft with almost no snow and very little cloud ice. The trends in runs dry0 and dry0sn- are the same as in the 26 January runs but to a lesser degree do to the higher convective fractions and lack of large anvil in the 23 February simulations. Run dry0 does show some reduction in graupel and a significant increase in snow (Fig. 10f), but graupel remains the dominant ice species in run dry0. In run dry0sn- snow and graupel are of similar magnitude with graupel dominant nearer the freezing level (Fig. 10g). The sequential water-then-ice saturation scheme used in this run does limit the cloud liquid water aloft especially above 8 km. Combined with the increase in cloud ice in this region, this likely accounts for the slight decrease in graupel and increase in snow over run dry0.

f. Apparent heating (Q_1) profiles

Rainfall-normalized apparent heating profiles, including the convective and stratiform components, for both cases are shown in Fig. 11. The convective–stratiform separation was obtained using the scheme developed for the GCE model (Lang et al. 2003) and not the one used earlier to derive the convective fractions. The 26 January case is divided into an early stage, which is dominated by the convective region (Fig. 11a), and a late stage that contains a sizeable stratiform component (Fig. 11b). The early stage profile (Fig. 11a) has strong heating throughout the column with a midlevel

maximum near 6 km, a very convective signature. The profiles from runs dry0 and dry0sn- are essentially identical to the control run profiles and are not shown. For the later period, the total heating profile remains positive, except near the surface, but the magnitude of heating is greatly reduced, especially at lower levels, and results in a heating profile with two nearly equal peaks centered at 5.5 and 9.5 km. The stratiform component is more prominent with significant cooling below 4 km and larger heating aloft. The total heating profiles from runs dry0 (Fig. 11c) and dry0sn- (not shown) are very similar to the control with minor changes in the magnitudes of the peaks. Thus, the overall heating is not affected by the changes to the microphysics. Below 5 km, the heating profile in run dry0 is nearly identical to the control run. However, there is an interesting change in the results from the separation algorithm. In run dry0, the amplitudes of the convective and stratiform profiles are amplified compared to those in the control run. There is more heating in the convective profile and more cooling in the stratiform profile but no difference in the net. Eliminating the high-density ice in the anvil region reduced the area of 40-dBZ echo. This has the effect of reducing the convective region as determined by the separation algorithm. As a consequence, some of the evaporative cooling below the melting layer that previously was assigned as convective is now properly categorized as stratiform. This was one of the key issues addressed by Lang et al. (2003) and has implications for latent heating retrieval algorithms that rely on rainfall-normalized convective and stratiform profiles such as the Goddard convective–stratiform heating (CSH) algorithm (Tao et al. 1993a, 2000, 2001). But, these changes in hydrometeor type will also affect the microwave or radar signatures and in turn other algorithms that rely on these synthetic data to retrieve heating from CRM simulations (e.g., Olson et al. 1999; Shige et al. 2004).

Normalized heating profiles for 23 February over the first 360 min of simulation time are shown in Figs. 11d,e for the 1000- and 250-m base microphysics runs, respectively. Again, the total heating profiles are nearly invariant, including those from runs dry0 and dry0sn- (not shown), and dominated by heating throughout the column. Unlike 26 January there is a strong heating peak at very low levels near 2 km in addition to the midlevel peak at 5 km. The low-level peak is due to shallow, nonprecipitating clouds and is larger in the 250-m run.

5. Summary and conclusions

The 3D GCE model was used to simulate two convective cases, 26 January and 23 February 1999, repre-

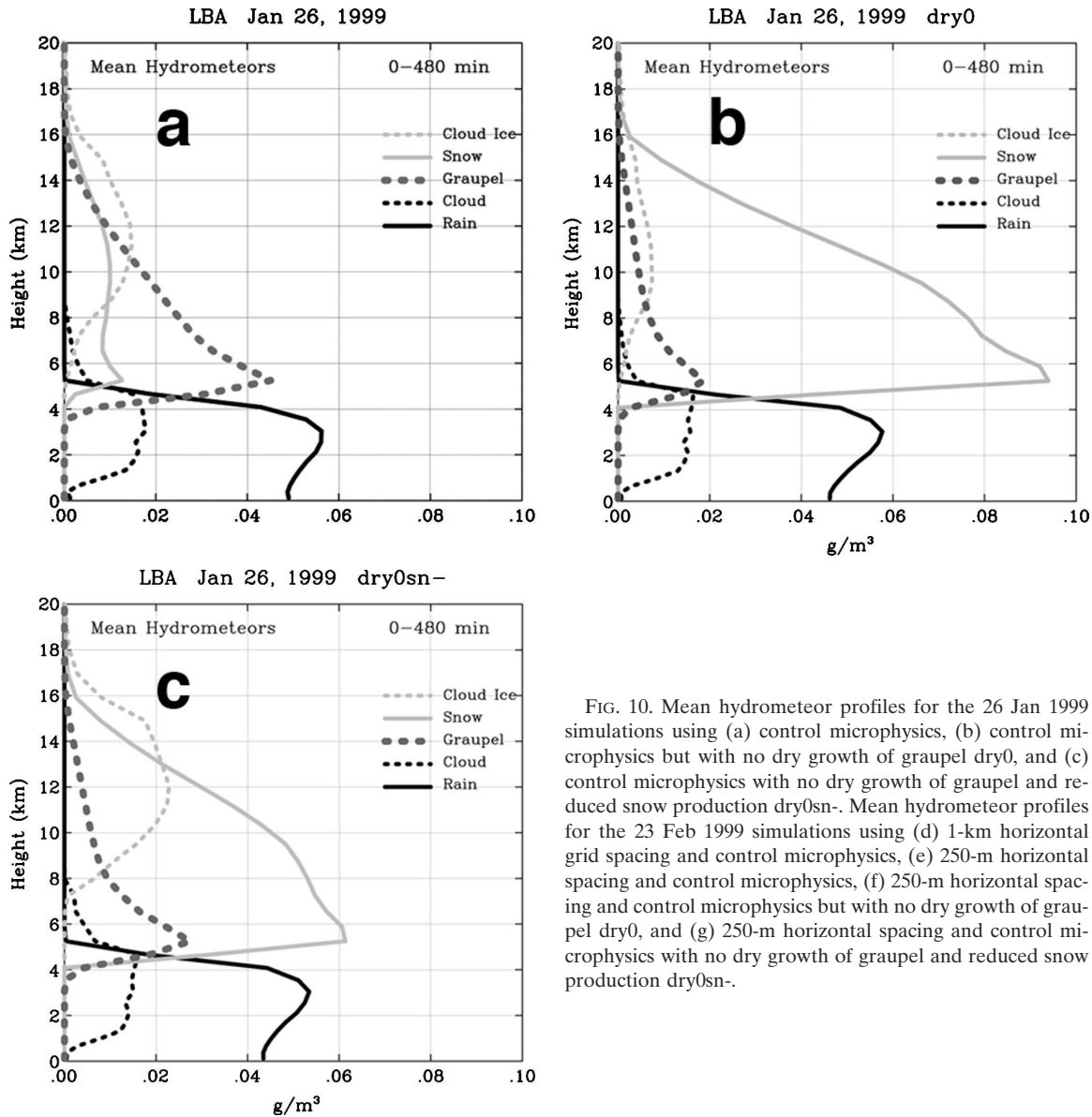


FIG. 10. Mean hydrometeor profiles for the 26 Jan 1999 simulations using (a) control microphysics, (b) control microphysics but with no dry growth of graupel dry0, and (c) control microphysics with no dry growth of graupel and reduced snow production dry0sn-. Mean hydrometeor profiles for the 23 Feb 1999 simulations using (d) 1-km horizontal grid spacing and control microphysics, (e) 250-m horizontal spacing and control microphysics, (f) 250-m horizontal spacing and control microphysics but with no dry growth of graupel dry0, and (g) 250-m horizontal spacing and control microphysics with no dry growth of graupel and reduced snow production dry0sn-.

senting two distinct convective regimes, easterly and westerly, respectively, that were observed during TRMM LBA. The model, applied in its native form, was able to capture the basic organization and structure of the convection associated with each of the two cases. This was primarily achieved because of the model's ability to link the convective organization to the observed environmental wind shear and instability. However, by improving various aspects of the simulations that might otherwise have been deficient in representing these cases, much more realistic simulations were achieved that better matched the observed characteristics of these systems.

The diurnal growth of convection on 23 February was

greatly improved by increasing the model's horizontal grid resolution from a typical application of 1 km to a much finer resolution of 250 m. Without the finer horizontal resolution, the model had a tendency to form deep convection abruptly, similar to the problem in larger-scale models. However, simulations using 250-m resolution resulted in a gradual transition from shallow to deep convection that occurred over a period of 3 h, much closer to the observed diurnal growth characteristics.

Model-simulated hydrometeor contents were made substantially more realistic as a result of improvements to the model's bulk microphysics. These improvements were primarily realized as a result of close, careful sta-

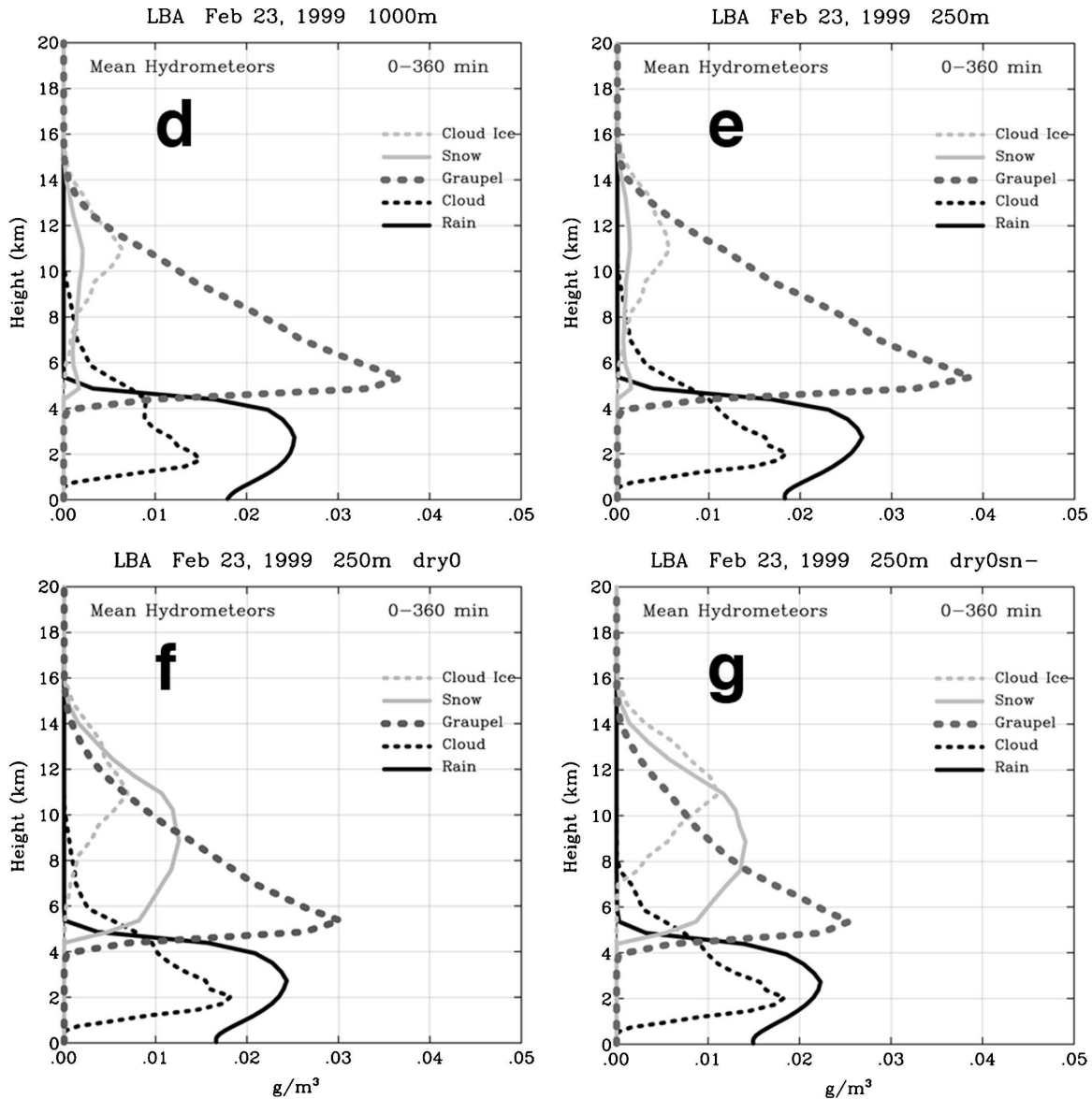


FIG. 10. (Continued)

tistical comparisons with radar observations but also through the calculation of brightness temperatures and information from aircraft observations. Appropriate periods were selected from the model to compare with radar-based CFADs and rainfall histograms by calculating model convective fractions just as was done in the radar analyses and as close to the resolution of the radar grids as possible. The unrealistic presence of high-density ice throughout the anvil was removed by eliminating the dry growth of graupel in the Rutledge and Hobbs (1984) three-class ice scheme. Comparisons of model-simulated reflectivities with radar values using CFADs showed that the elimination of dry growth

improved the model results, but the overall reflectivity distribution was still shifted too high as a result of the large snow amounts generated in the absence of dry growth. The excessive snow contents were reduced by lowering the collection efficiency of cloud ice by snow from 0.1 to 0.01 and the collection efficiency of cloud water by snow from 1.0 to 0.5. In addition, an alternate saturation scheme was used that produces less liquid cloud water aloft. Reducing the collection efficiency of cloud water by snow by far had the greatest impact on the snow amount. Lowering the cloud-ice collection efficiency and the use of the alternate saturation scheme had almost no effect on the excessive snow contents.

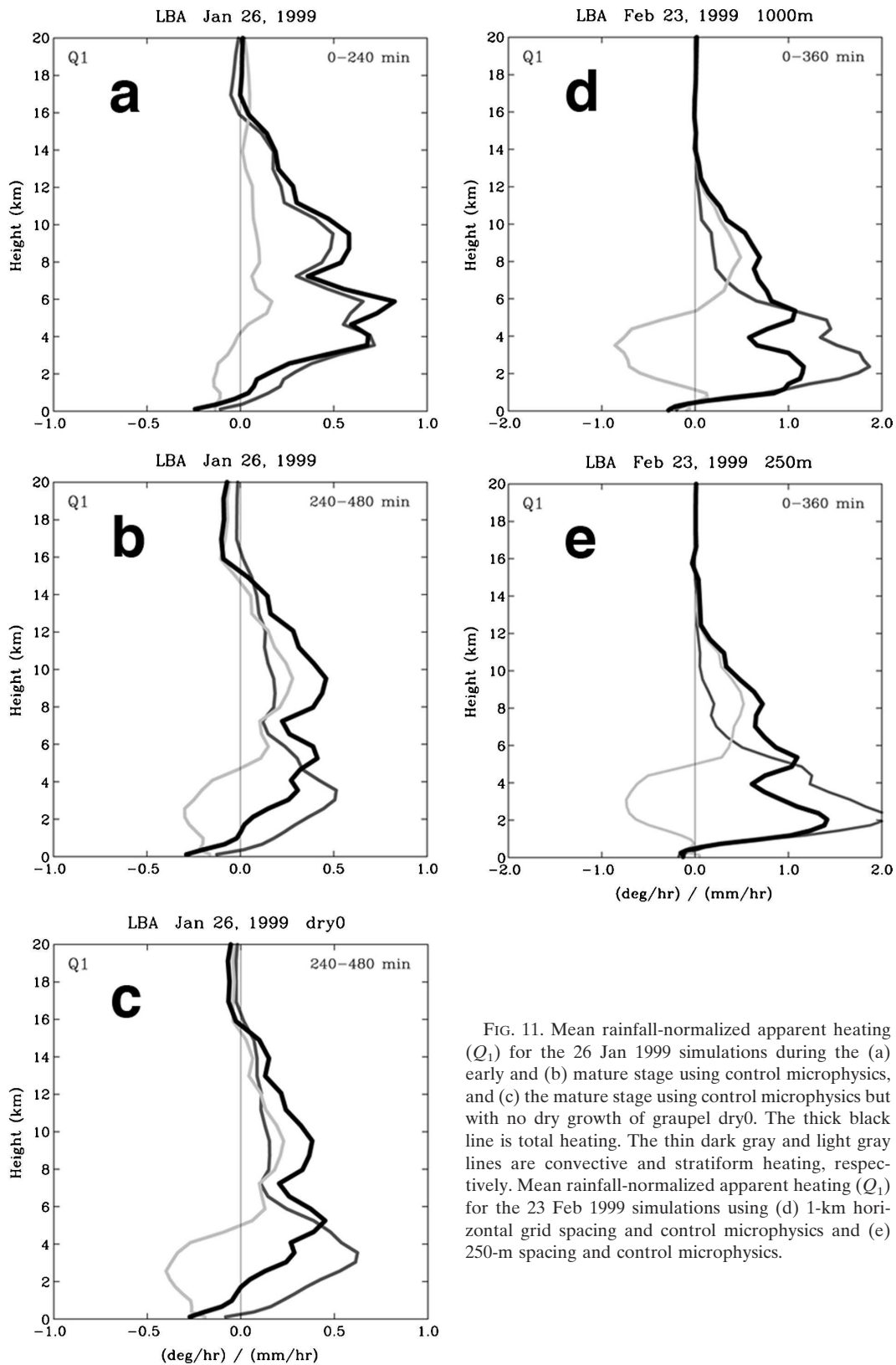


FIG. 11. Mean rainfall-normalized apparent heating (Q_1) for the 26 Jan 1999 simulations during the (a) early and (b) mature stage using control microphysics, and (c) the mature stage using control microphysics but with no dry growth of graupel dry0. The thick black line is total heating. The thin dark gray and light gray lines are convective and stratiform heating, respectively. Mean rainfall-normalized apparent heating (Q_1) for the 23 Feb 1999 simulations using (d) 1-km horizontal grid spacing and control microphysics and (e) 250-m spacing and control microphysics.

Reflectivity CFAD comparisons showed further gains with this setup. These changes to the microphysics were also manifest in improved brightness temperatures with the modified physics, resulting in more realistic ice scattering signatures than the base physics. However, coupled with the fact that the overall convective updraft intensity seemed to be well represented by the model, it appears that the overall transfer of cloud-sized particles to precipitation-sized ice particles is still too efficient. In addition to further reducing the collection efficiencies, adjustments to the Bergeron process offer another possible means of mitigating this problem and merit further study. Krueger et al. (1995) noted that the Bergeron term associated with the transfer of cloud ice to snow is allowed to operate even in the absence of liquid cloud water. Although Krueger et al. (1995) felt that this may act as a crude cloud-ice sedimentation, it would be far more realistic to limit the Bergeron process in the absence of cloud water and include a parameterization for cloud ice fall speeds (e.g., Hong et al. 2004). Cloud-ice sedimentation was not included in the short-term simulations in this study, but it could be very important for long-term simulations due to the interaction with radiation. Because 26 January had a large, coherent anvil and 23 February did not, the microphysics adjustments had much more impact on the 26 January simulations. These adjustments had the added benefit of increasing the size of the simulated stratiform region for 26 January, which appeared far too narrow in the base run. The reflectivity CFAD analysis for 26 January also showed that the model overestimated rain evaporation at low levels, a likely artifact of the one-moment microphysics scheme.

CFAD comparisons between model drafts and those from dual-Doppler analyses showed that the overall intensity of convection in each case was well represented by the model. Differences at lower levels are likely due to the use of a downward integration technique in the Doppler analyses. Rainfall histograms based on the radar observations were also used to compare with the model results. For 26 January, there was a distinct shift in the model histograms using the modified microphysics that effectively reduced the frequency of rain rates above 5 mm h^{-1} . The effects were minimal for 23 February due to the lack of a large stratiform area. The model consistently underestimated the occurrence of heavy rain rates in both cases and is consistent with the over evaporation. The inability of a one-moment microphysical scheme to handle size sorting leads to the overproduction of small drops at the expense of large drops.

Vertical profiles of model-simulated hydrometeor contents showed a distinct and realistic shift in the dom-

inant form of precipitation ice aloft from graupel to snow as a result of eliminating the dry growth of graupel for the 26 January case. Efforts to reduce the resulting excessive snow amounts led to more cloud ice in the upper part of the anvil in better agreement with aircraft data. Graupel was the main form of ice in all of the 23 February simulations as a result of higher convective fractions, but the proportion of snow to graupel was increased without the dry growth of graupel.

Total apparent heating profiles were shown to be rather insensitive to the changes in microphysics and horizontal resolution. However, changes to the convective and stratiform components implied that the separation algorithm did a better job, especially for the 26 January simulations, as a result of the more realistic simulations. This improved convective–stratiform separation and the improved realism of the ice contents aloft can have a positive impact on latent heating retrievals by providing a more realistic mapping between the hydrometeor and heating structures.

Further improvements to the 23 February and similar cases with weak shear might be achieved by using a coupled model with interactive fluxes obtained from a land surface model. Model artifacts associated with size sorting are difficult to overcome with a one-moment scheme. Thus, a two-moment scheme for both ice and liquid may be required and would serve as a good compromise over even more expensive spectral-bin schemes that have a very limited 3D application at this stage. Because of their relative economy, bulk microphysics will remain an important component of CRMs and as such improvements to these schemes are therefore of great value. The improvements proposed in this study should be generally applicable to other cases in other environments; however, as detailed comparisons with radar observations were only performed on these two LBA cases to date, further examples are needed to broaden or at least establish the scope of their applicability. In any event, the value of rigorous comparisons with observational data cannot be overstated. Radar is a natural fit for CRMs. Together with in situ measurements it can provide a tangible assessment of the collective accuracy of the parameterized physics. For without verification from such comparisons, even the use of much more sophisticated parameterizations may only result in cloud datasets that contain more expensive mistakes.

Acknowledgments. This research was supported by the NASA Headquarters Atmospheric Dynamics and Thermodynamics Program and the NASA TRMM. The authors are grateful to Dr. R. Kakar at NASA headquarters for his support of this research and to Lisa

Nalborczyk for help in preparing the final figures. Acknowledgment is also made to the NASA Goddard Space Flight Center for computer time used in this research.

REFERENCES

- Adler, R. F., H.-Y. M. Yeh, N. Prasad, W.-K. Tao, and J. Simpson, 1991: Microwave simulations of a tropical rainfall system with a three-dimensional cloud model. *J. Appl. Meteor.*, **30**, 924–953.
- Alexander, G. D., and G. S. Young, 1992: The relationship between EMEX mesoscale precipitation feature properties and their environmental characteristics. *Mon. Wea. Rev.*, **120**, 554–564.
- Barnes, G. M., and K. Sieckman, 1984: The environment of fast- and slow-moving tropical mesoscale convective cloud lines. *Mon. Wea. Rev.*, **112**, 1782–1794.
- Bechtold, P., J.-P. Chaboureaud, A. Beljaars, A. K. Betts, M. Kohler, M. Miller, and J.-L. Redelsperger, 2004: The simulation of the diurnal cycle of convective precipitation over land in a global model. *Quart. J. Roy. Meteor. Soc.*, **130**, 3119–3137.
- Betts, A. K., and C. Jakob, 2002: Evaluation of the diurnal cycle of precipitation, surface thermodynamics, and surface fluxes in the ECMWF model using LBA data. *J. Geophys. Res.*, **107**, 8045, doi:10.1029/2001JD000427.
- , J. D. Fuentes, M. Garstang, and J. H. Ball, 2002: Surface diurnal cycle and boundary layer structure over Rondônia during the rainy season. *J. Geophys. Res.*, **107**, 8065, doi:10.1029/2001JD000356.
- Chong, M., P. Amayenc, G. Scialom, and J. Testud, 1987: A tropical squall line observed during the COPT 81 experiment in West Africa. Part I: Kinematic structure inferred from dual-Doppler radar data. *Mon. Wea. Rev.*, **115**, 670–694.
- Chou, M.-D., and L. Kouvaris, 1991: Calculations of transmission functions in the IR CO₂ and O₃ Bands. *J. Geophys. Res.*, **96**, 9003–9012.
- , and M. J. Suarez, 1999: A shortwave radiation parameterization for atmospheric studies. NASA Tech. Memo. 15(104604), 40 pp.
- , W. Ridgeway, and M.-H. Yan, 1995: Parameterizations for water vapor IR radiative transfer in both the middle and lower atmospheres. *J. Atmos. Sci.*, **52**, 1159–1167.
- , K.-T. Lee, S.-C. Tsay, and Q. Fu, 1999: Parameterization for cloud longwave scattering for use in atmospheric models. *J. Climate*, **12**, 159–169.
- Cifelli, R., W. A. Petersen, L. D. Carey, S. A. Rutledge, and M. A. F. da Silva Dias, 2002: Radar observations of the kinematic, microphysical, and precipitation characteristics of two MCSs in TRMM LBA. *J. Geophys. Res.*, **107**, 8077, doi:10.1029/2000JD000264.
- , L. D. Carey, W. A. Petersen, and S. A. Rutledge, 2004: An ensemble study of wet season convection in the southwest Amazon: Kinematics and implications for diabatic heating. *J. Climate*, **17**, 4692–4707.
- Fu, Q., and K.-N. Liou, 1993: Parameterization of the radiative properties of cirrus clouds. *J. Atmos. Sci.*, **50**, 2008–2025.
- Gamache, J. F., and R. A. Houze Jr., 1982: Mesoscale air motions associated with a tropical squall line. *Mon. Wea. Rev.*, **110**, 118–135.
- Grabowski, W. W., and Coauthors, 2006: Daytime convective development over land: A model intercomparison based on LBA observations. *Quart. J. Roy. Meteor. Soc.*, **132**, 317–344.
- Guichard, F., and Coauthors, 2004: Modelling the diurnal cycle of deep convection over land with cloud-resolving models and single-column models. *Quart. J. Roy. Meteor. Soc.*, **130**, 3139–3172.
- Halverson, J. B., T. Rickenbach, B. Roy, H. Pierce, and E. Williams, 2002: Environmental characteristics of convective systems during TRMM LBA. *Mon. Wea. Rev.*, **130**, 1493–1509.
- Herdies, D. L., A. da Silva, M. A. F. Silva Dias, and R. Nieto Ferreira, 2002: Moisture budget of the bimodal pattern of the summer circulation over South America. *J. Geophys. Res.*, **107**, 8075, doi:10.1029/2001JD000997.
- Heymtsfield, A., A. Bansemer, P. R. Field, S. L. Durden, J. L. Stith, J. E. Dye, W. Hall, and C. A. Grainger, 2002: Observations and parameterizations of particle size distributions in deep tropical cirrus and stratiform precipitating clouds: Results from in situ observations in TRMM field campaigns. *J. Atmos. Sci.*, **59**, 3457–3491.
- Hong, S.-Y., J. Dudhia, and S.-H. Chen, 2004: A revised approach to ice microphysical processes for the bulk parameterization of clouds and precipitation. *Mon. Wea. Rev.*, **132**, 103–120.
- Houze, R. A., Jr., 1977: Structure and dynamics of a tropical squall-line system. *Mon. Wea. Rev.*, **105**, 1540–1567.
- Klemp, J. B., and R. B. Wilhelmson, 1978: The simulation of three-dimensional convective storm dynamics. *J. Atmos. Sci.*, **35**, 1070–1096.
- Kratz, D. P., M.-D. Chou, M. M.-H. Yan, and C.-H. Ho, 1998: Minor trace gas radiative forcing calculations using the k-distribution method with one-parameter scaling. *J. Geophys. Res.*, **103**, 31 647–31 656.
- Krueger, S. K., Q. Fu, and K. N. Liou, 1995: Improvements of an ice-phase microphysics parameterization for use in numerical simulations of tropical convection. *J. Appl. Meteor.*, **34**, 281–287.
- Kummerow, C., W. S. Olson, and L. Giglio, 1996: A simplified scheme for obtaining precipitation and vertical hydrometeor profiles from passive microwave sensors. *IEEE Trans. Geosci. Remote Sens.*, **34**, 1213–1232.
- , and Coauthors, 2000: The status of the Tropical Rainfall Measuring Mission (TRMM) after two years in orbit. *J. Appl. Meteor.*, **39**, 1965–1982.
- Lang, S., W.-K. Tao, J. Simpson, and B. Ferrier, 2003: Modeling of convective–stratiform precipitation processes: Sensitivity to partitioning methods. *J. Appl. Meteor.*, **42**, 505–527.
- , —, —, and —, 2004: Reply. *J. Appl. Meteor.*, **43**, 962–965.
- Leary, C. A., and R. A. Houze Jr., 1979: The structure and evolution of convection in a tropical cloud cluster. *J. Atmos. Sci.*, **36**, 437–457.
- LeMone, M. A., E. J. Zipser, and S. B. Trier, 1998: The role of environmental shear and thermodynamic conditions in determining the structure and evolution of mesoscale convective systems during TOGA COARE. *J. Atmos. Sci.*, **55**, 3493–3518.
- Lin, Y.-L., R. D. Farley, and H. D. Orville, 1983: Bulk parameterization of the snow field in a cloud model. *J. Climate Appl. Meteor.*, **22**, 1065–1092.
- Moncrieff, M., S. Krueger, D. Gregory, J.-L. Redelsperger, and W.-K. Tao, 1997: GEWEX Cloud System Study (GCSS) Working Group 4: Precipitating convective cloud systems. *Bull. Amer. Meteor. Soc.*, **78**, 831–845.
- Mugnai, A., H. J. Cooper, E. A. Smith, and G. J. Tripoli, 1990:

- Simulation of microwave brightness temperatures of an evolving hail storm at the SSM/I frequencies. *Bull. Amer. Meteor. Soc.*, **71**, 2–13.
- , E. A. Smith, and G. J. Tripoli, 1993: Foundations for statistical–physical precipitation retrieval from passive microwave satellite measurements. Part II: Emission-source and generalized weighting-function properties of a time-dependent cloud-radiation model. *J. Appl. Meteor.*, **32**, 17–39.
- Olson, W. S., C. D. Kummerow, Y. Hong, and W.-K. Tao, 1999: Atmospheric latent heating distributions in the Tropics derived from passive microwave radiometer measurements. *J. Appl. Meteor.*, **38**, 633–664.
- , P. Bauer, C. D. Kummerow, Y. Hong, and W.-K. Tao, 2001: A melting layer model for passive/active microwave remote sensing applications. Part II: Simulation of TRMM observations. *J. Appl. Meteor.*, **40**, 1164–1179.
- , and Coauthors, 2006: Precipitation and latent heating distributions from satellite passive microwave radiometry. Part I: Improved method and uncertainties. *J. Appl. Meteor. Climatol.*, **45**, 702–720.
- Panegrossi, G., and Coauthors, 1998: Use of cloud model microphysics for passive microwave-based precipitation retrieval: Significance of consistency between model and measurement manifolds. *J. Atmos. Sci.*, **55**, 1644–1673.
- Petch, J. C., A. R. Brown, and M. E. B. Gray, 2002: The impact of horizontal resolution on the simulation of convective development over land. *Quart. J. Roy. Meteor. Soc.*, **128**, 2031–2044.
- Petersen, W. A., S. W. Nesbitt, R. J. Blakeslee, R. Cifelli, P. Hein, and S. A. Rutledge, 2002: TRMM observations of intraseasonal variability in convective regimes over the Amazon. *J. Climate*, **15**, 1278–1294.
- Pielke, R. A., and Coauthors, 1992: A comprehensive meteorological modeling system—RAMS. *Meteor. Atmos. Phys.*, **49** (1–4), 69–91.
- Rickenbach, T. M., and S. A. Rutledge, 1998: Convection in TOGA COARE: Horizontal scale, morphology, and rainfall production. *J. Atmos. Sci.*, **55**, 2715–2729.
- , R. N. Ferreira, J. B. Halverson, D. L. Herdies, and M. A. F. Silva Dias, 2002: Modulation of convection in the southwestern Amazon basin by extratropical stationary fronts. *J. Geophys. Res.*, **107**, 8040, doi:10.1029/2000JD000263.
- Rotunno, R., J. B. Klemp, and M. L. Weisman, 1988: A theory for strong, long-lived squall lines. *J. Atmos. Sci.*, **45**, 463–485.
- Rutledge, S. A., and P. V. Hobbs, 1984: The mesoscale and microscale structure and organization of clouds and precipitation in midlatitude cyclones. Part XII: A diagnostic modeling study of precipitation development in narrow cold-frontal rainbands. *J. Atmos. Sci.*, **41**, 2949–2972.
- , R. A. Houze Jr., M. I. Biggerstaff, and T. Matejka, 1988: The Oklahoma–Kansas mesoscale convective system of 10–11 June 1985: Precipitation structure and single-Doppler radar analysis. *Mon. Wea. Rev.*, **116**, 1409–1430.
- Shige, S., Y. N. Takayabu, W.-K. Tao, and D. E. Johnson, 2004: Spectral retrieval of latent heating profiles from TRMM PR data. Part I: Development of a model-based algorithm. *J. Appl. Meteor.*, **43**, 1095–1113.
- Silva Dias, M. A. F., and Coauthors, 2002a: Cloud and rain processes in a biosphere-atmosphere interaction context in the Amazon Region. *J. Geophys. Res.*, **107**, 8072, doi:10.1029/2001JD000335.
- , and Coauthors, 2002b: A case study of convective organization into precipitating lines in the Southwest Amazon during the WETAMC and TRMM-LBA. *J. Geophys. Res.*, **107**, 8078, doi:10.1029/2001JD000375.
- Simpson, J., R. F. Adler, and G. North, 1988: A proposed Tropical Rainfall Measuring Mission (TRMM) satellite. *Bull. Amer. Meteor. Soc.*, **69**, 278–295.
- , C. Kummerow, W.-K. Tao, and R. Adler, 1996: On the Tropical Rainfall Measuring Mission (TRMM). *Meteor. Atmos. Phys.*, **60**, 19–36.
- Smith, E. A., X. Xiang, A. Mugnai, and G. Tripoli, 1992: A cloud radiation model for spaceborne precipitation retrieval. *Extended Abstracts, Int. TRMM Workshop on the Processing and Utilization of the Rainfall Data Measured from Space*, Tokyo, Japan, Communications Research Laboratory, 273–283.
- , —, and G. J. Tripoli, 1994: Design of an inversion-based precipitation profile retrieval algorithm using an explicit cloud model for initial guess microphysics. *Meteor. Atmos. Phys.*, **54**, 53–78.
- Smith, P. L., 1984: Equivalent radar reflectivity factors for snow and ice particles. *J. Climate Appl. Meteor.*, **23**, 1258–1260.
- , C. G. Meyers, and H. D. Orville, 1975: Radar reflectivity factor calculations in numerical cloud models using bulk parameterization of precipitation. *J. Appl. Meteor.*, **14**, 1156–1165.
- Smolarkiewicz, P. K., 1983: A simple positive definite advection scheme with small implicit diffusion. *Mon. Wea. Rev.*, **111**, 479–486.
- , 1984: A fully multidimensional positive definite advection transport algorithm with small implicit diffusion. *J. Comput. Phys.*, **54**, 325–362.
- , and W. W. Grabowski, 1990: The multidimensional positive advection transport algorithm: Nonoscillatory option. *J. Comput. Phys.*, **86**, 355–375.
- Smull, B. F., and R. A. Houze Jr., 1985: A midlatitude squall line with a trailing region of stratiform rain: Radar and satellite observations. *Mon. Wea. Rev.*, **113**, 117–133.
- , and —, 1987a: Dual-Doppler radar analysis of a midlatitude squall line with a trailing region of stratiform rain. *J. Atmos. Sci.*, **44**, 2128–2148.
- , and —, 1987b: Rear inflow in squall lines with trailing stratiform precipitation. *Mon. Wea. Rev.*, **115**, 2869–2889.
- Soong, S.-T., and Y. Ogura, 1973: A comparison between axisymmetric and slab-symmetric cumulus cloud models. *J. Atmos. Sci.*, **30**, 879–893.
- , and —, 1980: Response of trade wind cumuli to large-scale processes. *J. Atmos. Sci.*, **37**, 2035–2050.
- Steiner, M., R. A. Houze Jr., and S. E. Yuter, 1995: Climatological characteristics of three-dimensional storm structure from operational radar and rain gauge data. *J. Appl. Meteor.*, **34**, 1978–2007.
- Stith, J. L., J. E. Dye, A. Bansemer, A. J. Heymsfield, C. A. Grainger, W. A. Petersen, and R. Cifelli, 2002: Microphysical observations of tropical clouds. *J. Appl. Meteor.*, **41**, 97–117.
- Sui, C.-H., K.-M. Lau, and X. Li, 1998: Radiative–convective processes in simulated diurnal variations of tropical oceanic convection. *J. Atmos. Sci.*, **55**, 2345–2357.
- Szejwach, G., R. F. Adler, I. Jobard, and R. A. Mack, 1986: A cloud model–radiative model combination for determining microwave Tb–rain rate relations. Preprints, *Second Conf. on Satellite Meteorology/Remote Sensing and Applications*, Williamsburg, VA, Amer. Meteor. Soc., 444–449.
- Tao, W.-K., and J. Simpson, 1993: The Goddard Cumulus En-

- semble Model. Part I: Model description. *Terr. Atmos. Oceanic Sci.*, **4**, 19–54.
- , —, S. Lang, M. McCumber, R. Adler, and R. Penc, 1990: An algorithm to estimate the heating budget from vertical hydrometeor profiles. *J. Appl. Meteor.*, **29**, 1232–1244.
- , —, C.-H. Sui, B. Ferrier, S. Lang, J. Scala, M.-D. Chou, and K. Pickering, 1993a: Heating, moisture and water budgets of tropical and midlatitude squall lines: Comparisons and sensitivity to longwave radiation. *J. Atmos. Sci.*, **50**, 673–690.
- , S. Lang, J. Simpson, and R. Adler, 1993b: Retrieval algorithms for estimating the vertical profiles of latent heat release: Their applications for TRMM. *J. Meteor. Soc. Japan*, **71**, 685–700.
- , J. Simpson, S. Lang, C.-H. Sui, B. Ferrier, and M.-D. Chou, 1996: Mechanisms of cloud–radiation interaction in the Tropics and midlatitudes. *J. Atmos. Sci.*, **53**, 2624–2651.
- , S. Lang, J. Simpson, W. S. Olson, D. Johnson, B. Ferrier, C. Kummerow, and R. Adler, 2000: Retrieving vertical profiles of latent heat release in TOGA COARE convective systems using a cloud resolving model, SSM/I and radar data. *J. Meteor. Soc. Japan*, **78**, 333–355.
- , and Coauthors, 2001: Retrieved vertical profiles of latent heating release using TRMM rainfall products for February 1998. *J. Appl. Meteor.*, **40**, 957–982.
- , and Coauthors, 2003: Microphysics, radiation and surface processes in the Goddard Cumulus Ensemble (GEC) model. *Meteor. Atmos. Phys.*, **82**, 97–137.
- Weisman, M. L., W. C. Skamarock, and J. B. Klemp, 1997: The resolution dependence of explicitly modeled convective systems. *Mon. Wea. Rev.*, **125**, 527–548.
- Williams, E., and Coauthors, 2002: Contrasting convective regimes over the Amazon: Implications for cloud electrification. *J. Geophys. Res.*, **107**, 8082, doi:10.1029/2001JD000380.
- Yang, G.-Y., and J. Slingo, 2001: The diurnal cycle in the Tropics. *Mon. Wea. Rev.*, **129**, 784–801.
- Yang, S., and E. A. Smith, 1999a: Moisture budget analysis of TOGA COARE area using SSM/I retrieved latent heating and large scale Q_2 estimates. *J. Atmos. Oceanic Technol.*, **16**, 633–655.
- , and —, 1999b: Four-dimensional structure of monthly latent heating derived from SSM/I satellite measurements. *J. Climate*, **12**, 1016–1037.
- , and —, 2000: Vertical structure and transient behavior of convective–stratiform heating in TOGA COARE from combined satellite-sounding analysis. *J. Appl. Meteor.*, **39**, 1491–1513.
- Yuter, S. E., and R. A. Houze Jr., 1995: Three-dimensional kinematic and microphysical evolution of Florida cumulonimbus. Part II: Frequency distributions of vertical velocity, reflectivity, and differential reflectivity. *Mon. Wea. Rev.*, **123**, 1941–1963.
- Zipser, E. J., 1977: Mesoscale and convective-scale downdrafts as distinct components of squall-line structure. *Mon. Wea. Rev.*, **105**, 1568–1589.